

**HELWAN UNIVERSITY**

**FACULTY OF COMPUTERS AND INFORMATION**

**COMPUTER SCIENCE DEPARTMENT**

# **Automatic Detection of Landmarks and Abnormalities in Eye Fundus Images**

---

**By**

**Ali Mohamed Nabil Allam**

**A dissertation submitted to the Faculty of Computers and Information in partial  
fulfillment of the requirements for the award of the degree of**

**Doctor of Philosophy in Computer Science**

## **Supervisors**

**Professor Aliaa Abdel-Halim Youssif**

Professor of Computer Science, Dean  
Faculty of Computers and Information  
Helwan University

**Professor Atef Zaki Ghalwash**

Emeritus Professor of Computer Science, Ex-Dean  
Faculty of Computers and Information  
Helwan University

**September 2016**

---

The research described in this dissertation was carried out at the Faculty of Computers & Information – Helwan University, Cairo, Egypt.

© 2016 by Ali Mohamed Nabil Allam.

[www.aliallam.net](http://www.aliallam.net)

ALL RIGHTS RESERVED. No part of this research shall be reproduced, in any form, or by any means, without permission in writing from the researcher.

## Abstract

---

The eye fundus is the only organ of the central nervous system of the human body that can be imaged directly since it can be seen through the pupil. Accordingly, experts have been applying digital image processing techniques to fundus images with the aim of identifying, locating, and analyzing the fundus landmarks such as the optic disc, macula, and blood vessels. Particularly, optic disc segmentation is a key element in automatic screening systems which facilitates the detection of lesions that affect the interior surface of the eye (i.e. fundus), such as glaucoma and diabetic retinopathy.

Therefore, this research aimed to provide a fully automated technique for detecting and segmenting the optic disc. This research reviewed, categorized and compared the optic disc detection algorithms and methodologies in the literature, giving a description of each of them, highlighting their key points and performance measures.

Having a concrete understanding of those previous studies, the proposed approach for segmenting the optic disc was presented. First, the fundus image was preprocessed in order to estimate the approximate location of the optic disc, excluding the positions that doubtfully contain the optic disc. Consequently, the top candidates for the optic disc were nominated and then ranked based on their strengths. Afterwards, the vessels density within each candidate was calculated and then weighted according to the candidate's strength, in which the top-scoring candidate was chosen to be the segmented optic disc.

The proposed algorithm was tested and evaluated over nine diverse datasets containing a total of 1933 images. The segmentation algorithm proved its effectiveness by segmenting the optic disc correctly in 1831 images achieving a total sensitivity of 94.72% which was comparable to the results achieved by the other approaches. But more importantly, the implementation of the segmentation algorithm was fully automated regardless of the extreme heterogeneity of the tested datasets; as no image-dependent parameters were adjusted, nor predefined templates were used for the sake of customizing the proposed algorithm over certain datasets.

## **Declaration**

---

I declare that the work in this dissertation was carried out in accordance with the *Regulations of Helwan University*. The work is original except where indicated by special reference in the text and no part of the dissertation has been submitted for any other degree.

The dissertation has not been presented to any other academic institute for examination either in the Arab Republic of Egypt or abroad.

**Ali M. N. Allam**

## List of Publications

---

### **In International Conference Proceedings:**

[1] A. M. N. Allam, A. A. Youssif, and A. Z. Ghalwash, "Optic Disc Segmentation by Weighting the Vessels Density within the Strongest Candidates," in *Proceedings of 2016 SAI Computing Conference*, pp. 91-99, London, United Kingdom, July 2016. DOI: 10.1109/SAI.2016.7555967  
Accessible at: <http://ieeexplore.ieee.org/document/7555967/>

### **In Peer-reviewed International Journal:**

[2] A. M. N. Allam, A. A. Youssif and A. Z. Ghalwash, "Automatic Segmentation of Optic Disc in Eye Fundus Images: A Survey," *Electronic Letters on Computer Vision and Image Analysis*, vol. 14, no. 1, pp. 1-20, Barcelona, Spain, September 2015. DOI: 10.5565/rev/elcvia.680  
Accessible at: <http://elcvia.cvc.uab.es/article/view/680>

## Acknowledgments

---

PREVIEW IS NOT AVAILABLE

# Table of Contents

---

List of Figures .....	ix
List of Tables .....	x
<b>CHAPTER 1. INTRODUCTION .....</b>	<b>1</b>
1.1. Ophthalmology Background .....	1
1.1.1. Eye Anatomical Structure .....	1
1.1.2. Imaging Modalities.....	2
1.1.3. Eye Fundus Image .....	4
1.2. Motivation of Fundus Image Processing.....	5
1.2.1. Automated Segmentation of Landmarks.....	5
1.2.2. Automated Detection of Abnormalities .....	6
1.3. Architecture of Fundus Image Processing.....	6
1.3.1. Fundus Image Datasets.....	8
1.3.2. Image Processing Functions.....	8
1.3.3. Processed Retinal Images .....	12
1.3.4. Evaluation Metrics .....	12
1.4. Research Work .....	13
1.4.1. Aims and Objectives of Research.....	13
1.4.2. Research Methodology.....	14
1.4.3. Organization of Dissertation .....	14
<b>CHAPTER 2. LITERATURE REVIEW.....</b>	<b>15</b>
2.1. Fundus Image Datasets .....	15
2.1.1. STARE.....	15
2.1.2. DRIVE.....	16
2.1.3. MESSIDOR.....	16
2.1.4. ONHSD.....	17
2.1.5. ARIA.....	17
2.1.6. ImageRet.....	17
2.1.7. DRIONS-DB.....	18
2.1.8. HRF .....	18
2.2. Evaluation Metrics.....	19

2.2.1. Sensitivity and Specificity.....	19
2.2.2. ROC Curve.....	20
2.2.3. Segmentation Accuracy.....	21
2.3. Preprocessing: Fundus Image Enhancement.....	22
2.3.1. Mask Generation .....	22
2.3.2. Conversion between heterogeneous datasets.....	23
2.3.3. Color Channels Processing.....	24
2.3.4. Color Normalization .....	25
2.3.5. Contrast Enhancement.....	27
2.3.6. Non-uniform Illumination Correction .....	30
2.4. Landmarks Segmentation.....	31
2.4.1. Motivation of Optic Disc Detection.....	32
2.4.2. Properties of the Optic Disc .....	32
2.4.3. Literature of Optic Disc Segmentation .....	33
2.5. Detection of Abnormalities .....	43
2.5.1. Motivation of Detecting Glaucoma and Diabetic Retinopathy .....	43
2.5.2. Clinical Indicators of Glaucoma .....	44
2.5.3. Clinical Indicators of Diabetic Retinopathy .....	48
2.5.4. Literature of Glaucoma Diagnosis.....	50
2.5.5. Literature of Diabetic Retinopathy Diagnosis .....	53
<b>CHAPTER 3. SYSTEM ARCHITECTURE .....</b>	<b>56</b>
<b>CHAPTER 4. EXPERIMENTAL RESULTS.....</b>	<b>57</b>
<b>CHAPTER 5. CONCLUSION AND FUTURE WORK.....</b>	<b>58</b>
<b>APPENDICES .....</b>	<b>59</b>
<b>OPHTHALMOLOGICAL GLOSSARY.....</b>	<b>60</b>
<b>REFERENCES .....</b>	<b>62</b>

## List of Figures

---

Figure 1-1. Anatomical structure of the human eye .....	2
Figure 1-2. Fundus photography .....	3
Figure 1-3. Images produced via fundus photography .....	3
Figure 1-4. Fluorescein / ICG angiography .....	3
Figure 1-5. Images produced via angiography.....	3
Figure 1-6. Fundus auto fluorescence (FAF).....	3
Figure 1-7. Images produced via FAF.....	3
Figure 1-8. Heidelberg Retina Tomography.....	4
Figure 1-9. Images produced via HRT.....	4
Figure 1-10. Images produced via OCT scan.....	4
Figure 1-11. Color fundus image .....	5
Figure 1-12. Architecture of fundus image processing.....	7
Figure 1-13. Scope of research work.....	13
Figure 2-1. Example of ROC curves .....	20
Figure 2-2. (a) A color image, (b) its corresponding mask, and (c) its excluded background .....	22
Figure 2-3. The FOV trigonometry used for the computation of the scale factor.....	24
Figure 2-4. (a) Full-color image split into its (b) red, (c) green and (d) blue channels .....	24
Figure 2-5. Effect of color normalization on abnormal retinal images.....	27
Figure 2-6. Effect of color normalization on retinal vessels.....	27
Figure 2-7. Contrast enhancement using HE and CLAHE.....	28
Figure 2-8. Local color contrast enhancement.....	29
Figure 2-9. Comparison between different techniques of contrast enhancement .....	30
Figure 2-10. Examples of non-uniform illumination.....	30
Figure 2-11. Illumination equalization.....	31
Figure 2-12. (a) Healthy fundus image (b) Diabetic fundus (containing exudates).....	32
Figure 2-13. (a) Normal optic disc (b) Glaucomatous optic disc .....	32
Figure 2-14. The cup and the rim of the optic disc.....	33
Figure 2-15. Sensitivity of OD detection algorithms over the DRIVE dataset.....	41
Figure 2-16. Sensitivity of OD detection algorithms over the STARE dataset .....	42
Figure 2-17. Sensitivity of OD detection algorithms over miscellaneous datasets .....	42
Figure 2-18. Sketch of the ISNT rule for the thickness of the neuroretinal rim .....	44
Figure 2-19. Optic disc splinter hemorrhages.....	45
Figure 2-20. Red-free optic disc image showing nerve fiber layer .....	46
Figure 2-21. Example of localized NFLD.....	46
Figure 2-22. Peripapillary atrophy.....	47
Figure 2-23. Abnormalities occurring in eye fundus due to diabetic retinopathy.....	49

## List of Tables

---

Table 1-1. Fundus images datasets.....	8
Table 2-1. Signal detection indices and derived evaluation metrics.....	19
Table 2-2. List of optic disc detection methods .....	39
Table 2-3. Glaucoma structural and functional indicators .....	47
Table 2-5. International clinical diabetic retinopathy disease severity scale.....	49
Table 2-4. List of glaucoma detection methods .....	52

# Chapter 1. Introduction

---

Ophthalmologists are able to diagnose eye diseases using images of the eye fundus which is photographed directly through the eye's pupil via a specialized low-power microscope with an attached camera. Thereby, computer vision systems are developed in order to localize and analyze fundus landmarks, namely the optic nerve head (i.e. neuroretinal rim and optic cup), the retinal blood vessels (i.e. arteries and veins), and the macular region (i.e. macula and fovea). This computer-aided image analysis, in turn, facilitates the detection of retinal lesions and abnormalities that result in slight-to-major changes of the eye fundus, such as exudates, aneurysms, hemorrhages, neovascularization, macular edema, notching, etc.

## 1.1. Ophthalmology Background

### 1.1.1. Eye Anatomical Structure

Fundus, Latin for the word "bottom", is an anatomical term referring to the portion of an organ opposite from its opening. Hence, the fundus of the eye is the interior surface of the eye, opposite the lens, and which includes the retina, optic disc, blood vessels, macula and fovea [1]. Moreover, the eye fundus is the only organ of the central nervous system of the human body that can be imaged directly since it can be seen and captured through the pupil of the eye [1], [2].

Therefore, numerous numbers of fundus images are analyzed by ophthalmologists all over the world, and over the past two decades, experts have been applying digital image processing techniques to ophthalmology with the main aim of improved diagnosis of various diseases that affect the eye such as glaucoma, diabetic retinopathy, neovascularization, age-related macular degeneration, arteriosclerosis, etc. [1], [2].

Figure 1-1 illustrates the anatomical structure of the human eye [3], in which some of the functions performed by the interior surface of the human eye are described below:

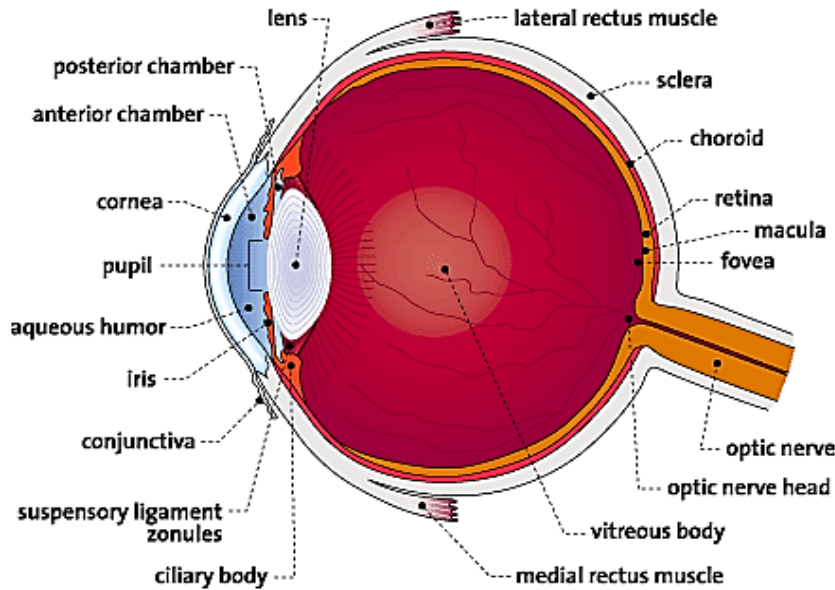


**Figure 1-1. Anatomical structure of the human eye**

- **Retina:** contains light sensitive cells called cones and rods, which are responsible for daytime and night vision, respectively; the retina is the tissue where the image is projected since it receives images formed by the lens and converts them onto signals that reach the brain by the means of the optic nerve.
- **Optic Nerve Head (ONH):** commonly referred to as the optic disc and sometimes as the optic papilla. It is a circular area where the optic nerve enters the retina coming from the brain, and which does not contain receptors itself, and is thereby the blind spot of the eye.
- **Macula and Fovea:** the macula it is a part of the eye close to the center of the retina which allows us to see objects with great detail. The fovea is a depression in the retina that contains only cones (not rods), and which provides accurate focused eyesight.
- **Blood Vessels:** like the rest of the human body, arteries and veins are the two main types of blood vessels responsible for the eye's blood supply. Arteries carry fresh blood from the heart and lungs to the eye while veins take away the blood that has been used by the eye and return it to the lungs and heart to be refreshed with oxygen and other nutrients [4].

### 1.1.2. Imaging Modalities

An imaging modality, in general, is an imaging system which uses a particular technique in order to detect different physical signals arising from a patient and produce images. The following modalities belong to the broad category of ophthalmological photography [5], [6]:

- **Color Fundus Photography:** the interior surface of the eye (i.e. retina, vasculature, optic disc and macula) is captured using a specialized low-power microscope with an attached camera. Moreover, in stereo fundus photography, image intensities represent the amount of reflected light from two or more different view angles for depth resolution.

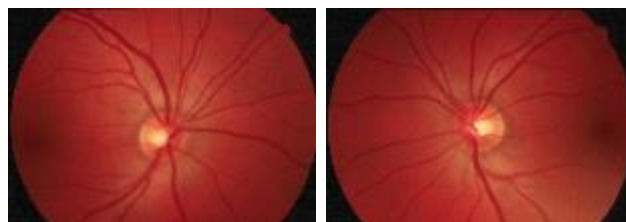
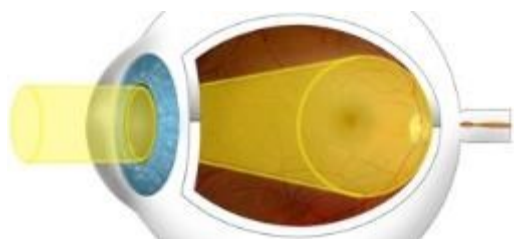


Figure 1-2. Fundus photography

Figure 1-3. Images produced via fundus photography

- **Fluorescein Angiography (FA) / Indocyanine Green Angiography (ICG):** a grayscale image in which the blood flow within both, the retina and the choroid, is captured by injecting fluorescein dye and indocyanine dye, respectively, in the blood vein.

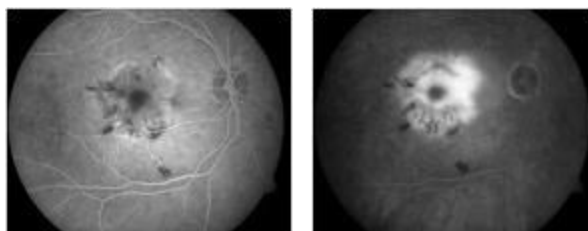
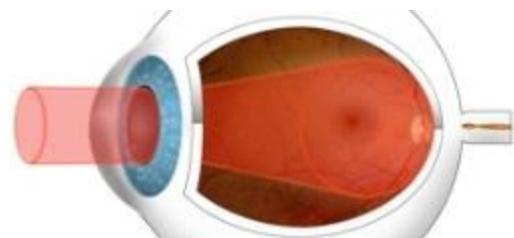


Figure 1-4. Fluorescein / ICG angiography

Figure 1-5. Images produced via angiography

- **Fundus Auto Fluorescence (FAF):** illuminating the retina with blue light causes certain cellular components to glow without injecting any dye.

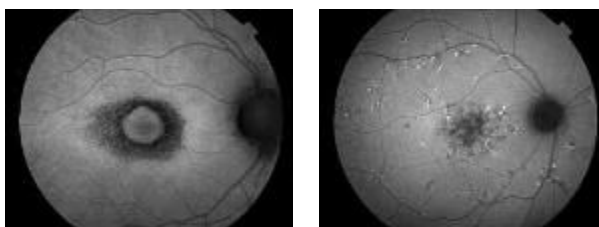
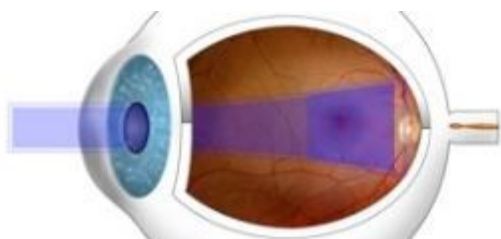


Figure 1-6. Fundus auto fluorescence (FAF)

Figure 1-7. Images produced via FAF

- **Confocal Scanning Laser Ophthalmoscopy (CSLO):** commercially, this imaging modality is known as Heidelberg Retina Tomography (HRT). It uses a special laser beam that is focused on the surface of the optic nerve in order to precisely capture a 3D image of the optic disc and the surrounding retina. HRT is a powerful diagnostic tool for glaucoma in particular.

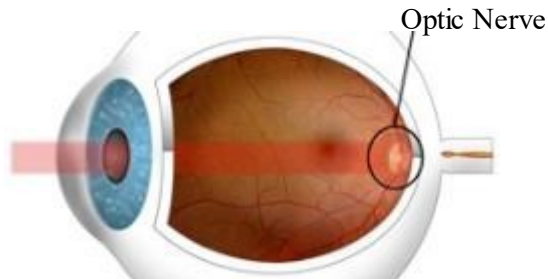


Figure 1-8. Heidelberg Retina Tomography

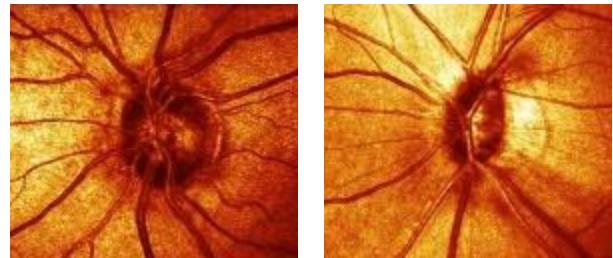


Figure 1-9. Images produced via HRT

- **Optical Coherence Tomography (OCT):** it is analogous to ultrasound except that it utilizes light instead of sound. OCT scan is used to capture the thickness of the retinal tissue by measuring the flight time of the originated backscatter. Thus, it is not considered a “*fundus imaging*” modality [5].

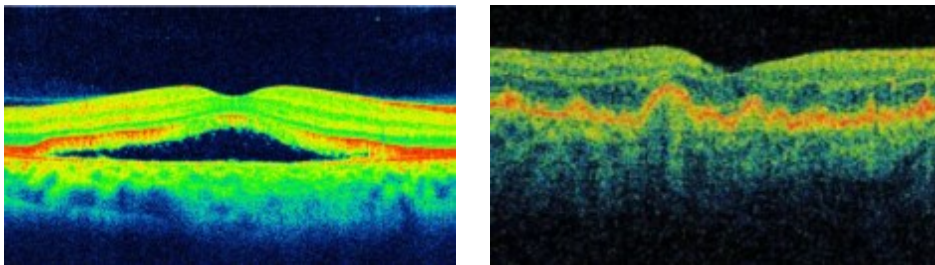
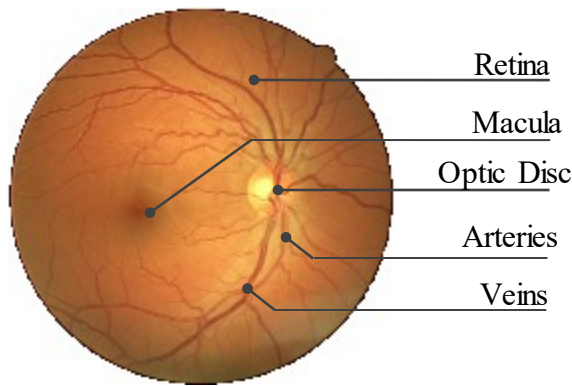


Figure 1-10. Images produced via OCT scan

### 1.1.3. Eye Fundus Image

While the function performed by each part of the fundus was described in section 1.1.1, the following text briefly describes the semblance and characteristics of each of these fundus landmarks. Figure 1-11 shows a labeled color fundus image of a healthy normal human eye (i.e. without lesions), produced via color fundus photography.



**Figure 1-11. Color fundus image**

- **Retina:** the color of the retina varies naturally according to the color of the light employed; however, the color of the fundus may be described as ranging from orange to vermillion [2].
- **Optic Nerve Head/ Optic Disc:** it is located towards the left-side or the right-side of a fundus image. It is round or vertically oval in shape, measuring about one-tenth to one-sixth the fundus diameter (about 2mm). It typically appears as a bright yellowish or whitish area where large blood vessels are found in the vicinity of the optic disc [2], [7].
- **Macula & Fovea:** the fovea, which falls at the center of the area known as the macula, is an oval-shaped, blood vessel-free reddish spot. It is approximately 5mm away from the center of the optic disc (equal to about 2.5 times the diameter of the optic disc) [2].
- **Blood Vessels:** the major branches of the retinal vasculature originate from the center of the optic disc to the four quadrants of the retina. In the macular region, all the vessels arch around, sending only small branches towards the vascular fovea area. The arteries appear with a brighter red color and are slightly narrower than the veins [2].

## 1.2. Motivation of Fundus Image Processing

The majority of works dealing with fundus image processing can be classified into two broad categories:

### 1.2.1. Automated Segmentation of Landmarks

The process of locating and subdividing an image into its constituent regions or objects is called segmentation. Hence, the eye fundus is being segmented in order to locate and isolate the fundus landmarks, namely the optic disc, macular region, and retinal blood vessels.

- **Optic disc segmentation:** the optic disc is a key landmark in retinal images, and shows changes related to diseases including glaucoma and diabetic retinopathies [8]. The optic disc also serves as a landmark in order to locate other fundus features such as the macula and central blood vessels [7] as discussed earlier in section 1.1.3.
- **Macula segmentation:** locating the macula is important in detecting related diseases such as age-related macular degeneration and macular edema [9].
- **Vasculature segmentation:** analyzing the shape, size, and color of the blood vessels in the retina is important for detecting diseases of blood circulation such as neovascularization, arteriosclerosis and occlusion.

### 1.2.2. Automated Detection of Abnormalities

Identifying the abnormalities within the eye fundus assists ophthalmologists to diagnose, predict and monitor the progress of, the disease that a patient suffers from.

- **Disease diagnosis:** refers to detecting the abnormal symptoms in the retina such as exudates, aneurysms and hemorrhages in order to diagnose diseases that affect the eye such as diabetic retinopathy, glaucoma, macular edema, etc.
- **Disease prediction:** refers to the early observation of retinal disorders that may lead to other serious pathological conditions or vision loss (blindness).
- **Disease progress monitoring:** concerned with comparing the changes of the states in the eye fundus at particular intervals of time in order to observe either the improvement or deterioration of some disease.

## 1.3. Architecture of Fundus Image Processing

Figure 1-12 overviews the high-level architecture of fundus image processing showing the data which is employed, the steps which are followed and the procedures which are applied in processing the eye fundus images.

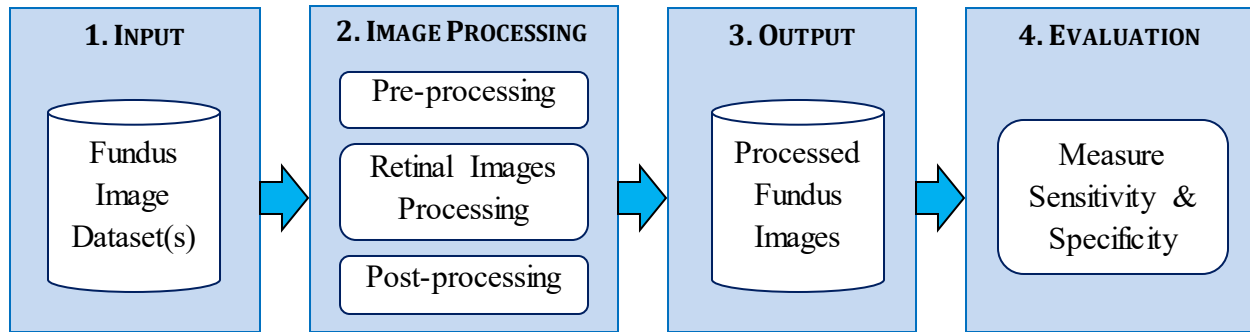


**Figure 1-12. Architecture of fundus image processing**

Each of the four modules of the shown architecture is briefly described below, and then discussed in detail in the subsequent sections:

- Input – retinal image datasets (section 1.3.1): refers to one set or more of retinal images that form the input data to be processed.
- Image processing (section 1.3.2): this is the backbone of the system architecture which is composed usually of three sub-processes in order to manipulate the dataset of the raw retinal images and convert it to a set of meaningful images (e.g. diagnosing a retinal image that suffers from a particular disease):
  - i. Preprocessing: a preliminary step that normally aims to enhancing the input image (e.g. contrast, sharpness and illumination of the image).
  - ii. Retinal images processing: the main objective of processing the retinal image normally aims to the segmentation of the image which is the process of isolating particular regions of interest within the image [10]. Regions of interest (ROI) may include retinal abnormalities (e.g. exudates, hemorrhages, aneurysms, etc.), and may also include the retinal landmarks (e.g. optic disc, macula, and vascular tree) as discussed earlier at section 1.2.
  - iii. Post-processing: refers to the last processing step that aims to describing, marking or classifying (i.e. annotating) the objects that were segmented in the fundus image.
- Output – processed retinal images (section 1.3.3): the output dataset which refers to the retinal images after being enhanced, processed and then annotated.
- Evaluation (section 1.3.4): the accuracy of experimental results is usually measured by two main metrics, sensitivity and specificity.

### 1.3.1. Fundus Image Datasets

Table 1-1 shows a chronological list of the most widely used datasets of fundus images employed for image processing, which will be reviewed in detail at section 2.1, in the next chapter. The table differentiates between each dataset and another from the perspective of: the size of the dataset, field of view (FOV), images size, images format and the ground truth provided with the dataset.

The ground truth provides the means of comparing and evaluating the experimental results achieved by some algorithm using the true results provided usually by medical experts (i.e. ophthalmologists) for an image dataset.

**Table 1-1. Fundus images datasets**

<b>Dataset Name, (Release Date)</b>	<b>Dataset Size</b>	<b>FOV</b>	<b>Image Size (pixels)</b>	<b>Images Format</b>	<b>Ground Truth</b>
STARE, (2000) [11]	397 images	35°	700×605	PPM	Blood Vessels and Optic Disc
DRIVE, (2004) [12]	40 images (two sets)	45°	565×584 (both sets)	TIFF	Blood Vessels
MESSIDOR, (2004) [13]	1200 images (three sets)	45°	Set (1): 1440×960 Set (2): 2240×1488 Set (3): 2304×1536	TIFF	Retinopathy Grading and Macular Edema (Hard Exudates)
ONHSD, (2004) [14]	99 images	45°	760×570	BMP	Optic Disc
ARIA, (2006) [15], [16]	143 images (three sets)	50°	768×576	TIFF	Vessels, Optic Disc and Fovea
ImageRet, (2008) [17]	Diaretdb0: 126 images Diaretdb1: 89 images	50°	1500×1152	PNG	Microaneurysms, Hemorrhages, and Hard & Soft Exudates
DRIONS-DB, (2008) [18]	110 images	-	600×400	JPG	Optic Disc
HRF, (2009) [19]	45 images (three sets)	45°	3504×2336 (all three sets)	JPG	Blood Vessels

### 1.3.2. Image Processing Functions

As mentioned before, image processing is the main module of the system architecture which includes three sub-components in order to manipulate the dataset of the captured retinal images

and convert it to a set of meaningful images. The input image is first enhanced, then segmented, and finally annotated. Software packages such as MATLAB® [20], OpenCV® [21], and ImageJ® [22] provide powerful means for implementing these image processing functions. The following part briefly overviews the main image processing functions that can be used for the enhancement and segmentation of images, which will be discussed later in details at Chapter 2 within the context of the literature review.

### **Step (1) – Preprocessing: Image Enhancement**

Image enhancement is the initial process of manipulating a raw image so that the result would be more suitable than the original for a specific application or further processing [10]. Below are some of the major enhancements that can be applied either solely or combined together with one another:

- i. Color image processing:** since the captured fundus image is a full-color image, it is obvious that color image processing techniques are strongly needed. For example, color splitting can be used to view and process each of the red, green, blue channels independently from one another [23]. Also conversion between the RGB and HSI color models is very useful in many situations; since the HSI model decouples the color (chromaticity) and gray-scale (intensity) information, therefore it is sometimes more useful to process an image using the HSI color model rather than the RGB model [10].
- ii. Contrast enhancement:** when the contrast of the captured image is too low, it is difficult to detect and isolate objects of interest. Therefore, brightening or darkening a low-contrast image can be achieved by stretching (spreading) the histogram of that image through approaches such as histogram equalization and histogram specification. Moreover, in order to stretch the contrast of a full-color image, it is logical to spread the color intensities uniformly, leaving the colors themselves unchanged; therefore, as mentioned in the previous paragraph, the HSI color space is ideally suitable for color histogram processing [10].
- iii. Luminosity equalization:** the non-uniform illumination in the retina makes the typical analysis of retinal images impractical and useless. Thus, in order to overcome the uneven illumination, each pixel of the image is corrected and equalized [7], [24].
- iv. Filtering:** spatial linear filters (e.g. mean filter) as well as non-linear filters (e.g. median filter) are used for image smoothing and noise removal. Conversely, first derivative filters (e.g. Prewitt and Sobel filters) as well as second derivative filters (e.g. Laplacian filter) are used for image sharpening (i.e. deblurring) as well as the detection of edges, lines and points. Moreover,

an image can be also filtered in the frequency domain in order to smoothen and sharpen it via using low-pass filters and high-pass filters, respectively [10].

- v. **Background subtraction:** masks are created and used to exclude the background of the image from further calculations and processing. In other words, only the pixels belonging to the semi-oval retina are included for processing [7].
- vi. **Morphological processing:** this technique can be applied as an image enhancement technique as well as an image segmentation technique. The two fundamental operations of morphological processing are dilation and erosion; in which dilation leads to thickening the original binary object, whereas erosion is an inverse procedure in which an object is thinned. Moreover, erosion and dilation can be applied together after one another and in a reversed order as well, in order to achieve opening and closing, respectively. Opening generally removes small objects from an image while preserving the shape and size of large objects in the image; whereas closing generally merges narrow breaks or gaps and eliminates small holes in the image [23], [10].
- vii. **Datasets conversion:** a scale factor is calculated and used to convert the spatial resolution between datasets with different field of views (FOVs). For instance, a scale factor of 0.76 is used to convert between the STARE and DRIVE datasets [24] which have FOVs of 35 and 45 degrees, respectively.

### Step (2) – Processing: Image Segmentation

As stated previously, the main objective of processing the fundus image typically aims to the segmentation of the objects within an image. Segmentation is an essential step prior to the classification and description of the lesions or landmarks in a fundus image. The main methods of image segmentation reviewed in the literature are:

- i. **Region-based methods:** the objective of such methods is to produce connected regions, based on similarity, that are as large as possible (i.e. produce as few regions as possible) allowing some flexibility within each region [23]. For example, region-growing, as its name implies, groups the seed pixels or sub-regions into larger similar regions based on predefined criteria of growth (such as specific ranges of color) [10].
- ii. **Boundary-based methods:** the objective of such methods is to determine a closed boundary, based on differences and discontinuities, such that an inside object (e.g. optic disc) and an outside boundary (edge) can be defined [23]. Gradient operators (e.g. Prewitt and Sobel

kernels), the Laplacian, Laplacian of Gaussian (LoG), Difference of Gaussians (DoG) and the Canny edge detector are some of the methods of detecting image boundaries (edges) [10], [25].

- iii. Color-based methods:** in order to segment an image based on color, the segmentation technique can be carried out on either the HSI color space or the RGB color space. It is intuitive to use the HSI space because color is conveniently represented in the hue plane (H), and saturation (S) is typically used as a masking image in order to isolate further regions of interest in the hue image, while the intensity (I) is used less frequently for segmentation of color images because it carries no color information. However, better results can be obtained using the RGB color vectors by measuring and comparing the Euclidean distance between an RGB pixel and a specified color range [10].
- iv. Active contour (snakes):** the main aim of active contour models or snakes is to evolve a curve in order to detect objects in an image. For instance, starting with an initial curve around the object to be segmented within an image, the curve (i.e. snake) is pulled toward nearby features (i.e. local minima) such as lines and edges, locating them accurately [26], [27].
- v. Matched filters:** a matched filter describes the expected appearance of a desired object or region of interest for purposes of comparative modeling. Thus, the segmentation process is carried out by isolating the region (pixels) having the least accumulated difference compared to the matched filter [7].
- vi. Thresholding:** an image is easily and speedily segmented by selecting a threshold which partitions images directly into regions based on intensity values and/or properties of these values. Global thresholding and local thresholding are two types of thresholding that may be applied to an image; global thresholding is a segmentation technique that uses a constant threshold over the entire image, whereas local (variable) thresholding uses a variable threshold that changes over an image based on the properties of a neighborhood (e.g. average intensities of a neighborhood) [10].
- vii. Morphological Watershed:** the watershed transform is a powerful segmentation tool that aims to isolate and separate the touching objects within an image. Segmenting an image via watershed is a two-step process; first, finding the markers and the segmentation criterion used to split the regions which is most often the contrast or gradient. Second, performing a marker-controlled watershed with these two elements in order to control over-segmentation [10], [28], [29].

### Step (3) – Post-processing: Image Description

After the eye fundus image has been enhanced and segmented, either the external boundary or the internal skeleton of the recognized region is marked, classified and annotated with the appropriate description, automatically.

#### 1.3.3. Processed Retinal Images

The processed retinal images constitute the output dataset which refers to the retina images after being enhanced, processed and then annotated. These processed retina images are compared to the ground truth in order to evaluate the accuracy of experimental work as explained in the following section.

#### 1.3.4. Evaluation Metrics

The experimental work is typically assessed using the sensitivity and specificity measures which are also sometimes referred to as recall and precision, respectively. Sensitivity is a measure that reflects the probability of a positive response for the cases in which the landmark or abnormality is present, whereas specificity is the probability of negative response for the cases in which the landmark or abnormality is absent. The higher the sensitivity and specificity values was, the better the diagnosis [17]. These two evaluation measures, sensitivity and specificity, can be computed as follows:

$$\text{Sensitivity} = \frac{T_P}{T_P + F_N} \quad \text{Equation 1-1}$$

$$\text{Specificity} = \frac{T_N}{T_N + F_P} \quad \text{Equation 1-2}$$

$T_P$  (true positive): correct response for detecting the presence of an artifact (i.e. hit).

$T_N$  (true negative): correct response for identifying the absence of an artifact (i.e. correct rejection).

$F_P$  (false positive): incorrect response for identifying the absence of an artifact (i.e. false alarm).

$F_N$  (false negative): incorrect response for detecting the presence of an artifact (i.e. miss).

$T_P + F_N$ : total number of artifacts that are present.

$T_N + F_P$ : total number of artifacts that are non-present.

### 1.4. Research Work

The research work proposed within this dissertation is concerned to be S.M.A.R.T. [30]; that is to be specific, measurable, achievable, relevant and time-constrained. The following figure highlights the scope of this research done within each stage of fundus image processing:

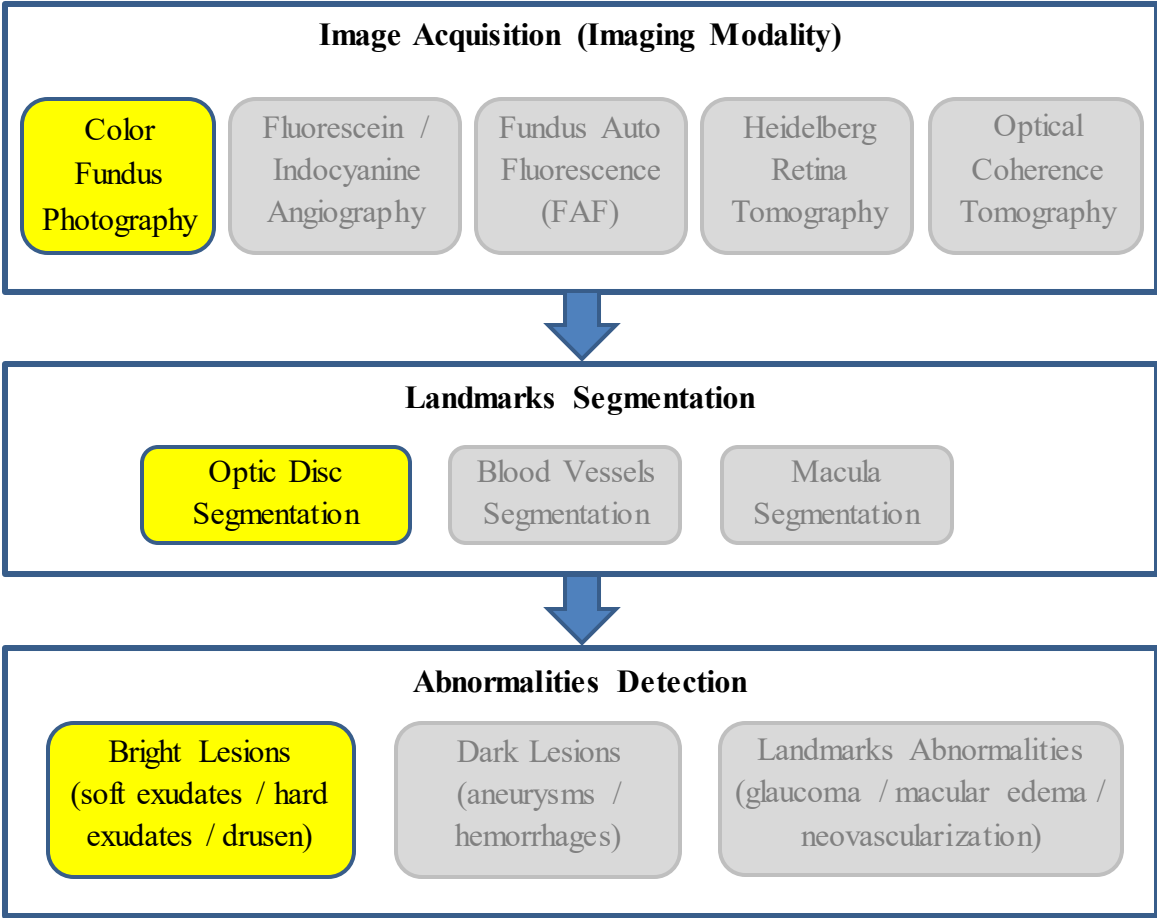


Figure 1-13. Scope of research work

#### 1.4.1. Aims and Objectives of Research

This research aims mainly to detect and segment one of the major landmarks in the fundus images which is the optic nerve head (i.e. optic disc). It also aims to the detection and early diagnosis (prediction) of particular lesions associated with the glaucoma disease which significantly change the general appearance and semblance of the optic nerve head. Therefore, in order to reach the aforementioned aims, the main objectives of this research are to:

- i. Employ a dataset of fundus images that act as a test bed on which digital image processing techniques are applied and assessed.

- ii. Exploit image processing techniques that enhance the original fundus images in order to make them more suitable for further image processing.
- iii. Investigate and propose image processing techniques in order to isolate and localize fundus landmarks, namely the optic disc.
- iv. Identify the abnormal features in the fundus with reference to the normal fundus anatomy in order to diagnose and predict the lesions that the retina suffers from.
- v. Measure the accuracy of the achieved results using the ground truth of the employed dataset in order to assess the proposed techniques compared to other ones.

### **1.4.2. Research Methodology**

The research methodology will be mainly based on employing many of the publicly available image datasets. The chosen datasets will act as a benchmark in order to provide robust evaluations and consistent comparisons against other methods using the ground truth accompanied with the dataset. The ground truth provides a means of evaluating the experimental results achieved by some algorithm using the true results provided usually by ophthalmologists on an image set.

### **1.4.3. Organization of Dissertation**

This research is organized into five main chapters followed by a glossary of the medical terminologies mentioned in the dissertation, and ended with the appendices that present additional information not directly included within the research, as well as a list of references cited in the research. Chapter 2 is mainly concerned with reviewing pertinent literature related to various aspects of medical image processing research, particularly in the field of ophthalmology. The chapter will review and compare the methods and algorithms used to enhance fundus images, as well as the techniques used for the detection of retinal abnormalities and the segmentation of retinal landmarks. Following the literature review, Chapter 3 presents the proposed system architecture and will describe each of its components along with the proposed methods, techniques and algorithms used to carry out and implement these components. Chapter 4 lays out the experimental results obtained during the course of this work. At the end of this research, Chapter 5 forms the conclusion obtained by the research and outlines a direction for the work that could be done in the future.

# Chapter 2. Literature Review

---

This chapter presents a review of the pertinent literature that runs along a parallel vein to this research. The literature review starts with presenting the most widely used image datasets, passing through the evaluation metrics used for segmentation assessment, and ending with a detailed review of the image preprocessing and segmentation approaches.

It presents the preprocessing methods used to enhance retinal images, followed by the main image processing methods for segmenting the key landmark of the eye fundus which is the optic disc. It also reviews the methods of detecting abnormalities occurring within the optic disc which in turn help in diagnosing retinal diseases such as glaucoma and diabetic retinopathy.

## 2.1. Fundus Image Datasets

The fundus images are considered the raw material to be enhanced, segmented and evaluated. The image datasets are normally accompanied with a ground truth which acts as a benchmark for comparing and evaluating the achieved experimental results using the true results of that image set. Table 1-1 provided a brief description of the most widely used publicly available datasets, which are described in more details in the following subsections:

### 2.1.1. STARE

- **Dataset description:** STARE dataset (Structured Analysis of the Retina) [11] contained 397 fundus images which were captured using a fundus camera with a field of view (FOV) of 35 degrees. Each image was of size of 700×605 pixels, in which the images were cropped at the top and the bottom of the FOV. It is worth to mention that the full dataset should have contained 402 images as described by the dataset manual, but only 397 images were included in the dataset, as images (47), (108), (109), (144) and (167) were missed out of the provided dataset.
- **Ground truth:** each image within the dataset was diagnosed by one or more of thirteen different diagnoses, in which blood vessel segmentation experimental work was provided including 20 hand-labeled images, along with the experimental results, and a demo. Also optic disc detection work including 81 images was also provided along with ground truth and the experimental results.

### 2.1.2. DRIVE

- **Dataset description:** DRIVE database (Digital Retinal Images for Vessel Extraction) [12] was mainly developed for segmentation of blood vessels in retinal images. The dataset contained 40 images in which 33 did not show any sign of diabetic retinopathy and 7 showed signs of mild early diabetic retinopathy. Each image was captured at  $565 \times 584$  pixels with a FOV of 45 degrees. For this database, the images were cropped around the FOV, and for each image, a mask image was provided in order to delineate the FOV.
- **Ground truth:** the set of 40 images was divided into a training set and a test set, each of which contained 20 images. For the training images, a single manual segmentation of the vasculature was provided. For the test cases, two manual segmentations were available: one to be used as gold standard, whereas the other one to be used for comparing computer-generated segmentations against those of an independent human observer. The DRIVE's website also provided a results page that listed results from some algorithms in a tabular format. The result browser is a useful way to explore the database by viewing images and segmentations for a small set of methods that has been implemented.

### 2.1.3. MESSIDOR

- **Dataset description:** MESSIDOR database [13] (Méthodes d'Evaluation de Systèmes de Segmentation et d'Indexation Dédiées à l'Ophthalmologie Rétinienne) was established to facilitate studies on computer-assisted diagnoses of diabetic retinopathy. The dataset contained 1200 images packaged in three sets. Each set was divided into four subsets, each of which containing 100 images in TIFF format. The images were captured using a camera with a 45-degree field of view at  $1440 \times 960$ ,  $2240 \times 1488$  and  $2304 \times 1536$  pixels. 800 images were acquired with pupil dilation (one drop of Tropicamide at 0.5%) and 400 images were captured without dilation.
- **Ground truth:** each set was associated with a spreadsheet that included two diagnoses: the retinopathy grade and the risk grade of macular edema, provided by medical experts for each image. The retinopathy grade was classified into four grades (grade 0, 1, 2 and 3) according to three main factors which were the number of microaneurysms, number of hemorrhages, and the neovascularization. On the other hand, hard exudates have been used to classify the risk of macular edema into three grades (grade 0, 1 and 2).

#### 2.1.4. ONHSD

- **Dataset description:** ONHSD dataset (Optic Nerve Head Segmentation Dataset) [14] contained 99 fundus images taken from both, the left and right eyes of 50 patients. It is observed that the dataset missed one right-eye image out of the 50 eye pairs. Besides, 96 images had discernible optic discs which were acquired using a fundus camera with a field angle lens of 45 degrees and size of 760×570 pixels.
- **Ground truth:** the center of the optic disc has been marked up by a clinician. Then, four clinicians marked the optic disc edge where it intersected with radial spokes (at 15 degree angles) radiating from the nominated center. These multiple nominations of the edge were used to characterize the degree of subjective uncertainty in the edge position.

#### 2.1.5. ARIA

- **Dataset description:** ARIA (Automated Retinal Image Analysis) [15], [16] aimed to provide an automated image analysis platform capable of predicting individuals at risk of eye disease. The dataset contained a total of 143 images collected by staff members of St. Paul's Eye Unit and the University of Liverpool as part of the ARIA project. The images were captured with a camera of FOV of 50 degrees at resolution of 768×576 and were stored as uncompressed TIFF files. The dataset was organized into three groups (i.e. subsets), including 23 images of age-related macular degeneration, 61 healthy images, and 59 diabetic images.
- **Ground truth:** Two image analysis experts traced out the blood vessels in the images of all three subsets. Besides, the locations of the optic disk and fovea were also outlined in 120 images within the healthy and diabetic subsets.

#### 2.1.6. ImageRet

- **Dataset Description:** ImageRet project [17] provided two datasets, DIARETDB0 and DIARETDB1, which were used for benchmarking diabetic retinopathy. The ImageRet datasets were made publicly available in 2008 using a digital fundus camera of 50° field of view in which each image was of size of 1500×1152 pixels in PNG format. The DIARETDB0 subset contained 126 fundus images, whereas DIARETDB1 contained 89 color fundus images. It is worth to mention that four images were missed out of the DIARETDB0 dataset (images 10, 17, 40 and 78), which was supposed to contain 130 images as mentioned in the dataset documentation.

- **Ground truth:** In the DIARETDB0 dataset, each fundus image had a corresponding text file that listed the types of abnormalities occurring in the image without providing more details (e.g. size, location, number of occurrences, etc.). Whereas, each fundus image in DIARETDB1 was associated with a corresponding xml file that represented the ground truth. The xml document showed all finding types occurring in an image, marked by four different experts with a certainty/confidence degree (i.e. high, medium, low), as well as their location coordinates. In both datasets, these finding types included the red small dots, hemorrhages, hard exudates, soft exudates, and neovascularization. Besides, the optic disc was occasionally marked by some of the experts within some images of DIARETDB1.

### 2.1.7. DRIONS-DB

- **Dataset description:** DRIONS-DB (Digital Retinal Images for Optic Nerve Segmentation Database) [18] was created for benchmarking optic nerve segmentation in fundus images. The images were acquired with a color analogical fundus camera, and they were digitized using a high-resolution scanner. The database was composed of 110 images of size of 600×400 pixels.
- **Ground truth:** For each image, two experts manually segmented the contour of the optic disc. Each contour was marked as a sequence of 36 points and was stored in a separate text file. A MATLAB script was provided to graphically show the experts' segmentations using the textual data stored in that text file.

### 2.1.8. HRF

- **Dataset description:** HRF (High-Resolution Fundus) image database [19] was established by a collaborative research group to support comparative studies on automatic segmentation algorithms on retinal fundus images, in order to help the evaluation of these algorithms which localize the macula, optic disc, or differentiate between arteries and veins. The database contained a total of 45 images divided into three sets; 15 images of healthy patients, 15 images of patients with diabetic retinopathy and 15 images of glaucomatous patients. Each image was of size of 3504×2336 pixels captured using a fundus camera with a field of view of 45 degrees. Also the binary masks determining field of view were provided.
- **Ground truth:** Each image, as mentioned above, was classified either as a normal fundus image, a diabetic fundus image, or a glaucomatous fundus image. Also, binary gold standard vessel segmentation images were available for each image.

## 2.2. Evaluation Metrics

Although the evaluation of an algorithm typically comes at the end stage of a detection or segmentation algorithm, yet the metrics used for evaluation are reviewed here in advance, in order to provide a concrete understanding of the results achieved by the segmentation algorithms in the literature which will be reviewed afterwards.

In medical diagnosis, the region of interest (e.g. landmark or lesion) is usually classified into two classes: present or absent; in which the response given by a human observer (expert) or a computer process is: positive or negative. Therefore, the detection of the abnormality or landmark is normally depicted in the terms presented in Table 2-1.

**Table 2-1. Signal detection indices and derived evaluation metrics**

	<b>Present ROI</b>	<b>Absent ROI</b>
<b>Positive Response</b>	Hit ( $T_P$ )	False alarm ( $F_P$ )
<b>Negative Response</b>	Miss ( $F_N$ )	Correct rejection ( $T_N$ )
	<b>SENS</b> = $\frac{T_P}{T_P + F_N}$	<b>SPEC</b> = $\frac{T_N}{T_N + F_P}$

The  $T_P$  and  $T_N$  indices refer to a correct response for identifying the presence and the absence of the ROI, respectively. Thus, the true positive index ( $T_P$ ) indicates the correct positive response of a human observer or computer for the ROI that is present within the retina, while the true negative index ( $T_N$ ) indicates the correct negative response for a ROI that is not present. Conversely, the  $F_P$  and  $F_N$  indices refer to an incorrect response. The false positive index ( $F_P$ ) indicates the incorrect positive response for the ROI that is not present, whereas the false negative index ( $F_N$ ) indicates the incorrect negative response for the ROI that is present. Derived from the four aforementioned indices as shown in Table 2-1, two main statistical metrics are computed in order to evaluate the detection of landmarks or abnormalities, which are: sensitivity and specificity.

### 2.2.1. Sensitivity and Specificity

Sensitivity is a measure that reflects the probability of a positive response for the cases in which the landmark or abnormality is present, whereas specificity is the probability of negative response for the cases in which the landmark or abnormality is absent. Both, sensitivity and specificity are expressed either as a proportion or a percentage given by the equation shown in Table 2-1, in which sensitivity is sometimes referred to as detection rate or true positive rate (TPR),

whereas specificity is sometimes referred to as the true negative rate (TNR). Moreover, the term false positive rate (FPR) is also used for the complement of specificity, computed as  $(1 - \text{specificity})$  [31].

### 2.2.2. ROC Curve

The Receiver Operating Characteristics (ROC), as its name implies, was historically developed to analyze classification accuracy in differentiating signal from noise in radar detection during World War II. The ROC test was then adapted, keeping its same naming, to many other domains that were heavily dependent on screening and diagnostic tests, such as medical imaging [32]. Although the sensitivity and specificity metrics are often considered as the fundamental measures of a computer-aided detection system, yet the ROC analysis is also a highly desirable measure because it requires a significantly smaller sample size of medical images compared to that needed to estimate sensitivity and specificity. Besides, another obstacle in an evaluation process is the availability of expert observers participating in the test. Accordingly, ROC curve is a method that measures performance without the need of expert observers and without large sample sizes [33].

As shown in Figure 2-1, the ROC is a curve that plots TPR (i.e. sensitivity) versus FPR (i.e.  $1 - \text{specificity}$ ), where the vertical axis (i.e. y-axis) for each ROC plot is labeled in terms of (sensitivity) from 0.0 to 1.0, while the horizontal axis (x-axis) is labeled in terms of  $(1 - \text{specificity})$  ranging from 0.0 to 1.0, which is also equivalent to labeling in terms of (specificity) decreasing from 1.0 to 0.0.

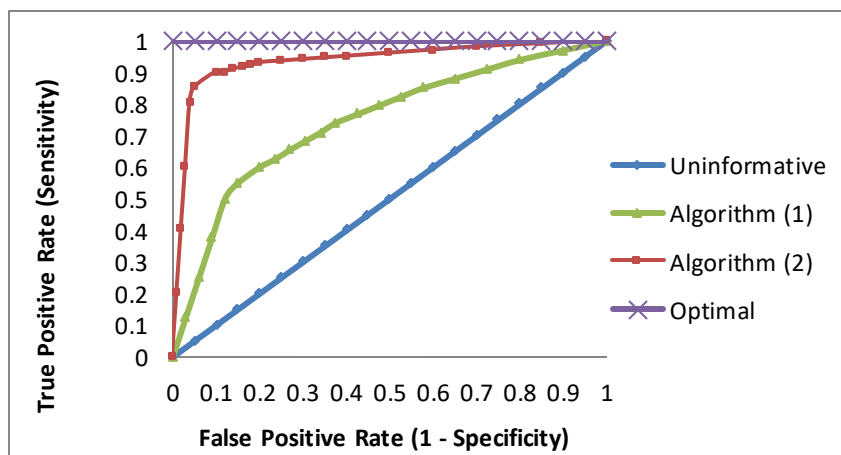


**Figure 2-1. Example of ROC curves**

The closer the ROC curve approaches to the top-left corner, the better the performance of the diagnosis system, since the most frequently-used performance metric extracted from the ROC

curve is the area under the curve (AUC) which ranges from 0.5 to 1.0, where 0.5 corresponds to random chance (i.e. uninformative) and corresponds to 1.0 for an optimal system [31], [33], [34].

### 2.2.3. Segmentation Accuracy

Typically, the spatial features of an object of interest such as its size, shape and area are the parameters that are commonly used in order to evaluate the segmentation accuracy of an object of interest. Moreover, these features also have clinical significance because they help in diagnosing diseases, as well as assessing the effect of treatment. Therefore, the main requirement needed to evaluate the segmentation results is the presence of the ground truth indicating the true features of the segmented object (i.e. its true size, shape or area). Thus, once the ground truth data is available, a variety of metrics can be used to evaluate the segmentation accuracy.

These evaluation metrics include the Hausdorff distance and the degree of overlap, which are relatively easy to compute and at the same time are not limited to certain geometrical patterns [33]. Other pixel-wise metrics such as the Euclidean distance is sometimes used to measure similarity, but the main drawback of such metric is that the similarity is estimated according to the distance between only two certain pixels such as the distance between the centroid of two optic discs.

#### (i) Hausdorff Distance

The intuition behind Hausdorff distance is to measure the similarity between two sets. So, if these sets have close Hausdorff distance, they are considered to look alike. Thereby, the Hausdorff distance  $h(A,B)$  is used to measure the similarity between two contours of the same object (e.g. optic disc), in which one contour  $A$  is defined by a human expert while the other contour  $B$  is generated by a computer process. The Hausdorff distance is computed as follows [33], [35].

Let  $A = \{a_1, a_2, \dots, a_m\}$  and  $B = \{b_1, b_2, \dots, b_m\}$  be the set of points on the two contours in which each point represents a pair of x and y coordinates. Then, the distance of a point  $a_i$  to the closest point on curve  $B$  is defined as

$$d(a_i, B) = \min_j \|b_j - a_i\| \quad \text{Equation 2-1}$$

Similarly, the distance of a point  $b_j$  to the closest point on curve  $A$  is given by

$$d(b_j, A) = \min_i \|a_i - b_j\| \quad \text{Equation 2-2}$$

Finally, the Hausdorff distance is the maximum of the above distances between the two contours.

$$h(A, B) = \max \left[ \max_i \{d(a_i, B)\}, \max_j \{d(b_j, A)\} \right] \quad \text{Equation 2-3}$$

## (ii) Overlap Score

The degree of overlap between two areas  $G$  and  $E$  encompassed by contours  $A$  and  $B$ , respectively, is defined as the ratio of the intersection and the union of these two areas, where  $G$  is the ground truth human-defined area and  $E$  is the experimental computer-generated area. The degree of overlap is computed as follows [33], [36], [37]:

$$OL = \frac{G \cap E}{G \cup E} \quad \text{Equation 2-4}$$

If there is an exact overlap between both contours, the ratio will be 1, whereas the ratio is given by 0 if there is no overlap between the two contours.

## 2.3. Preprocessing: Fundus Image Enhancement

Unfortunately, the raw digital fundus images are not always ready for immediate processing because of their poor quality due to factors such as the patient's movement and iris color, as well as imaging conditions such as non-uniform illumination. Therefore, an image should be first preprocessed in order to make it more suitable for further processing. The following subsections present the main preprocessing functions of fundus images.

### 2.3.1. Mask Generation

The captured fundus image consists of a semi-oval region of interest (ROI) on a dark background which is never really pure black (i.e. non-zero intensity). Therefore, masks are created and used in order to exclude the dark background of the image from further calculations and processing; in other words, only the pixels belonging to the semi-oval retinal fundus are included for processing. The mask image is a binary image in which the background pixels are assigned the value of "zero" and pixels within the ROI are assigned the value of "one", where the original color image is multiplied by the created mask image to produce a color image without noisy pixels in the background, while the ROI is left unchanged [7], [24], as shown in Figure 2-2.

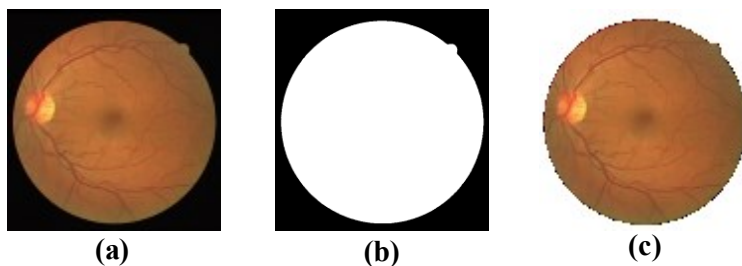


**Figure 2-2.** (a) A color image, (b) its corresponding mask, and (c) its excluded background

However, some of the publicly available retinal datasets, such as DRIVE, HRF, DIARETDB0 and DIARETDB1 are accompanied with these corresponding mask images, but most of the other datasets, as well as the real life images, do not include such mask images, and therefore the retinal images must be manipulated in some way in order to generate their corresponding masks.

For instance, in their procedure of detecting the anatomical structures in fundus images, Gagnon *et al.* [38] generated the mask image using pixel value statistics outside the ROI of the fundus image which were calculated for each of the three color bands. Consequently, a 4-sigma thresholding was applied such that pixels with intensity value above that threshold were considered to belong to the ROI. Finally, results for all bands were combined through logical operations and region connectivity test in order to identify the largest common connected mask, since ROI size was not always the same for each band due to different color response of the camera.

Also, Goatman *et al.* [39] automatically generated the masks by the simple thresholding of the green channel of the retinal image followed by a  $5 \times 5$  median filtering in order to exclude the dark surrounding region. On the other hand, ter Haar [24] created the mask by thresholding the red channel of the retinal image using a threshold value that was determined empirically, and then the thresholded image was morphologically processed via the opening, closing and erosion operators through a  $3 \times 3$  square kernel. In the same direction, Hashim *et al.* [40] generated the binary mask by convolving the red channel with a Gaussian low-pass filter, in which the resultant image was thresholded using Otsu's global threshold.

### **2.3.2. Conversion between heterogeneous datasets**

A digital fundus camera using a field of view (FOV) of  $35^\circ$ , such as the one used in the STARE dataset [11], displays a smaller area of the retina than a camera using a FOV of  $45^\circ$ , such as the one used in the DRIVE dataset [12], which is obviously smaller than that of DIARETDB1 whose FOV is  $50^\circ$  [17]. A scale factor computed by ter Haar [24] was used to convert the spatial resolution (i.e. magnification) between datasets having different field of views. The scale factor was based on the FOV-trigonometry illustrated in Figure 2-3:

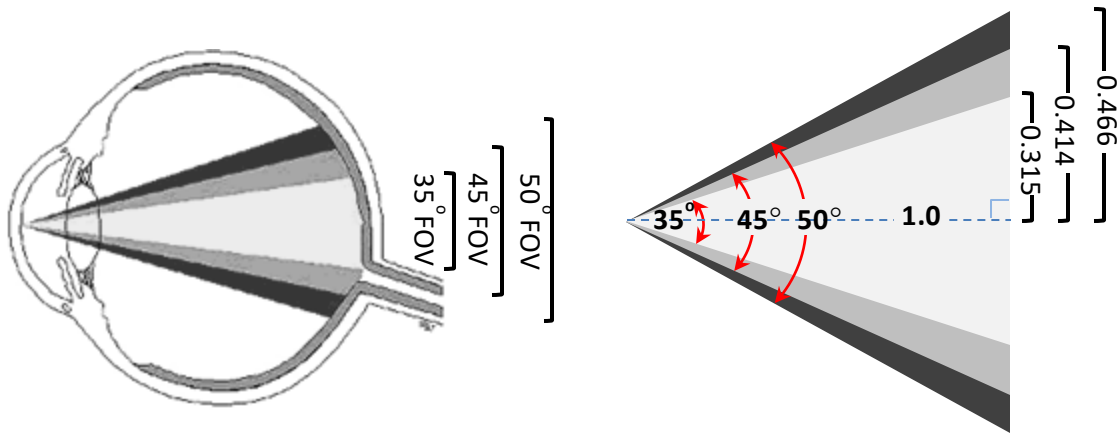


**Figure 2-3. The FOV trigonometry used for the computation of the scale factor**

Hence, the following equation was used to convert between images with 35° FOV (e.g. STARE) and 45° FOV (e.g. DRIVE), based on the trigonometry of the FOV:

$$scale = \frac{\tan(35/2)}{\tan(45/2)} = 0.76 \quad \text{Equation 2-5}$$

### 2.3.3. Color Channels Processing

The fundus color image consists of three color channels like any other image, in which the green channel has the highest contrast, whereas the red channel tends to be saturated and it is the brightest channel, while the blue channel tends to be empty [41], as noticed in Figure 2-4.

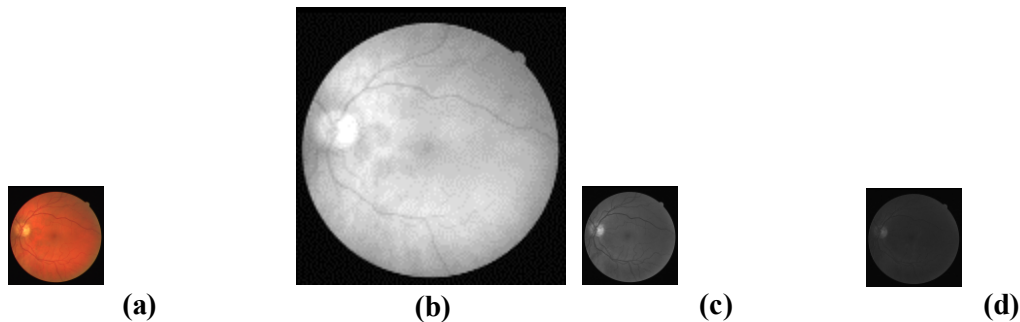


**Figure 2-4. (a) Full-color image split into its (b) red, (c) green and (d) blue channels**

Since it provides the highest contrast, the green channel was heavily used by most algorithms, discarding the red component in some cases which are so-called “red-free images” and ignoring the blue component in most of the algorithms. Therefore, the green channel was utilized for miscellaneous purposes such as detecting different retinal landmarks and several abnormalities due to its high contrast within retinal images. For instance, Goldbaum *et al.* [42] and Odstroilik *et al.* [19] convolved the green plane with matched filters with the purpose of segmenting retinal

blood vessels, while Yang *et al.* [43] utilized the green band to detect microaneurysms although they normally appear as small red spots. Also, Hoover and Goldbaum [41] located the optic disc using only the green band of the retinal image, whereas Staal *et al.* [12] used the green channel for the extraction of image ridges in color fundus images, while Niemeijer *et al.* [44] localized both the optic disc and fovea simultaneously using only the green plane of the color fundus image.

Moreover, Salem and Nandi [45] utilized the green channel image intensity as one of the feature components of the feature vector created for segmenting the retinal vessels. Similarly, Soares *et al.* [46] utilized the “inverted” green component to construct the feature vector. Related to the latter approach, many algorithms such as [47], [48], [49], [50], [51] exploited the “inverted green channel” so that the blood vessels appear brighter than the background.

However, even though the green channel was solely utilized in most approaches and for various purposes as mentioned in the previous paragraph, yet the red channel was also exploited sometimes in combination with the green band. For instance, Aquino *et al.* [37] observed that the optic disc appeared in the red field as a well-defined white shape, brighter than the surrounding area, and therefore, the optic disc segmentation was performed in parallel on the red and green bands and the better of the two segmentations was ultimately selected. Also, Al-Rawi *et al.* [52] showed that using the red band or even the blue band was comparable to using the green band in vessels segmentation with matched filtering. Moreover, Lu [36] and Hashim *et al.* [40] combined intensity information from the red and green channels together by calculating a modified intensity channel component using a weighted average, in which a higher weight was given to the red channel in order to keep the image variation across the optic disc boundary but suppress that across the retinal vessels.

#### **2.3.4. Color Normalization**

Another major preprocessing task in retinal images is color normalization which does not aim to find the true color of an image, but in fact color normalization algorithms transform the color of an image so as to be invariant with respect to the color of illumination, without losing the ability to differentiate between the objects or regions of interest [39]. The most commonly-used algorithms for color normalization are the gray-world normalization, comprehensive normalization, histogram equalization and histogram specification.

Gray-world normalization, also referred to as gray-world assumption algorithm, assumes that the changes in the illuminating spectrum can be modeled by three multiplicative constants applied

to the red, green and blue channels, respectively. The new color of any pixel is calculated by dividing each color channel by its respective mean value, removing the dependence on the multiplicative constant. Comprehensive normalization, a variation of the gray-world normalization proposed by Finlayson *et al.* [53], is a technique that iteratively applies chromaticity normalization followed by gray-world normalization for four or five iterations, until the change in values is less than a certain tolerance value.

On the other hand, histogram equalization is a non-linear transform applied individually to the red, green and blue bands of an image which affects the color perceived. It is considered to be a more powerful normalization transformation than the gray-world method. The results of histogram equalization tend to have an exaggerated blue channel and look unnatural due to the fact that in most images the distribution of the pixel values is usually more similar to a Gaussian distribution, rather than uniform [54].

Last but not least, histogram specification transforms the red, green and blue histograms to match the shapes of three specific histograms, rather than simply equalizing them, which results in more realistic images than those blue ones produced by equalization [39].

Both, Goatman *et al.* [39] and Youssif *et al.* [55] evaluated the effectiveness of the aforementioned methods of color normalization which aim to reduce color variations among different retinal images. According to Goatman's assessment, histogram specification was found to be the most effective normalization method in clustering and discriminating four different types of lesions, namely the cotton wool spots, hard exudates, blot hemorrhages, and drusen. Moreover, histogram specification had the advantage that it produced more realistic looking images since it did not exaggerate the contribution of the blue channel like the other methods, as shown in Figure 2-5, whereas comprehensive normalization was not found to perform much better than gray-world normalization in discriminating the lesions.

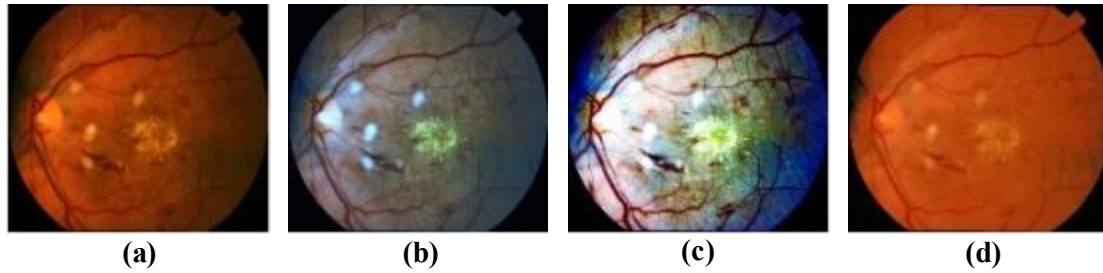


**Figure 2-5. Effect of color normalization on abnormal retinal images**

- (a) Reference image                      (b) Gray-world normalization  
(c) Histogram equalization              (d) Histogram specification

However, from a different perspective in evaluating normalization techniques as analyzed by Youssif *et al.* [55], histogram specification recorded the worst result in discriminating the vessels from non-vessels, while histogram equalization was found to be the most effective method by showing a clear separation between clusters of vessels and non-vessels, whereas comprehensive normalization, compared to gray-world normalization, showed more intense clusters and a narrower overlap between objects scattered in both clusters, as shown in Figure 2-6.

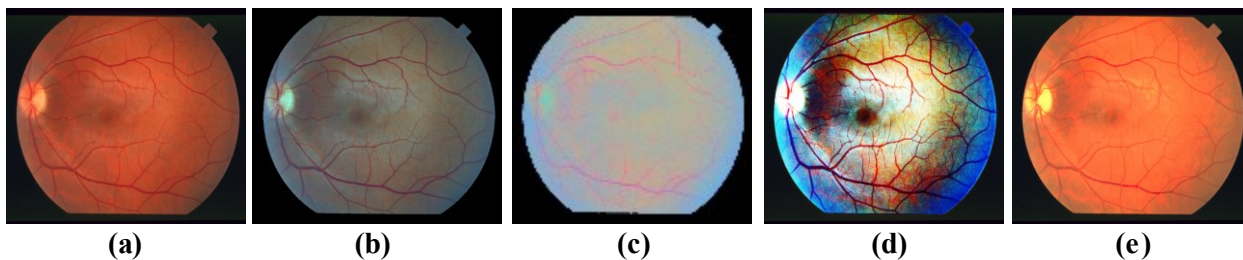


**Figure 2-6. Effect of color normalization on retinal vessels**

- (a) Reference image (STARE: im0255.ppm)  
(b) Gray-world normalization              (c) Comprehensive normalization  
(d) Histogram equalization                (e) Histogram specification

### 2.3.5. Contrast Enhancement

Contrast enhancement is the process of either darkening or brightening a low-contrast intensity image by spreading the range of intensities so that it spans the full range of intensity. Hence, some of the color normalization techniques, such as histogram equalization and histogram specification which were applied to the three color bands, may be also utilized to enhance the contrast of an image using one channel only, typically the green channel, the one which provides the highest contrast between vessels and non-vessels as mentioned before.

The main disadvantage of using histogram equalization (HE) in contrast enhancement is its dependence on the global statistics of an image, which may lead to noise amplification as well as the absence of some gray levels. This in turn results in a washed-out appearance in parts of the image due to over enhancement, while other parts around the periphery may not be enhanced enough [10], [56].

Adaptive histogram equalization (AHE) was applied by Wu *et al.* [57] and also exploited by Youssif *et al.* [7] in enhancing the contrast. AHE differs from the ordinary histogram equalization (HE) in the respect that the adaptive method computes several histograms, each of which corresponds to a distinct section of the image in order to redistribute the lightness values of the image. Therefore, it is suitable for improving the local contrast of an image and bringing out more detail, however noise may be still amplified as the ordinary histogram equalization.

Fadzil *et al.* [58], Krishnan *et al.* [59] and Maruthusivarani *et al.* [60] enhanced the contrast of the retinal image using contrast-limited adaptive histogram equalization (CLAHE) which is an improved variation of the AHE that limits the amplification of noise produced by the AHE.

Figure 2-7 illustrates the contrast of an image in the green band whose contrast was enhanced using histogram equalization (HE) and contrast-limited adaptive histogram equalization (CLAHE).

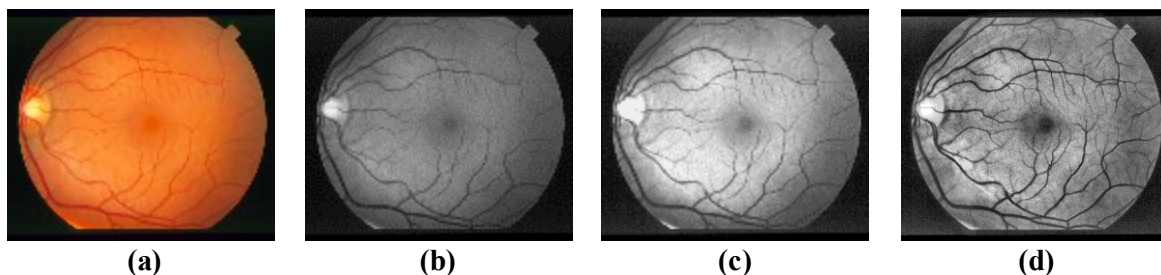


**Figure 2-7. Contrast enhancement using HE and CLAHE**

(a) Reference image (STARE: im0077.ppm)

(b) Green-band of (a)      (c) Histogram equalization of (b)      (d) CLAHE of (b)

Sinthanayothin *et al.* [61] presented a technique for enhancing the contrast of color images rather than intensity images using the adaptive local contrast enhancement, which was also utilized by Osareh *et al.* [62], ter Haar [24] and Park *et al.* [63]. This technique first transformed the components of the three color bands RGB into the HSI color model, which allowed the intensity component to be processed without affecting the perceived relative color values of the pixels. Consequently, the contrast of the intensity was enhanced by a locally adaptive transformation that

depended on the mean and standard deviation using a small running square window. Finally, the processed HSI image was converted back into an RGB image with an enhanced contrast. Figure 2-8, reproduced from Sinthanayothin [64], illustrates the effect of the local color contrast enhancement.

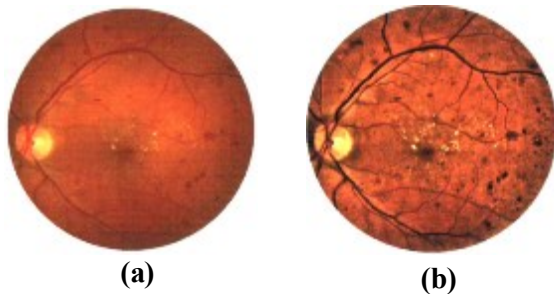


**Figure 2-8. Local color contrast enhancement**  
(a) Original image    (b) Contrast-enhanced color image

Rather than spreading the range of intensities in order to enhance the contrast, other more complex methods based on enhancing ridges, were exploited for contrast enhancement. For example, unsharp masking can increase either the sharpness or local contrast because both are forms of increasing differences between pixel values. Unsharp masking, based on spatial high-pass filtering, emphasizes high-frequency components of the image by subtracting an unsharp (blurred) version of the original image, which in turn improves the contrast, but amplifies the noise. However, Polesel *et al.* [65] proposed a technique that reduced noise amplification in digital images via adaptive unsharp masking.

Similar to the previous concept of increasing sharpness, each of the curvelet and contourlet transforms were used for enhancing edges. Both transforms differ from the wavelet transform in the respect of two additional features: directionality (i.e. the ability to capture different orientations) and anisotropy (i.e. the ability to capture smooth contours). Accordingly, the contourlet transform, presented by Do and Vetterli [66], was exploited by Feng *et al.* [67] and Rezatofghi *et al.* [68] in order to increase the contrast of blood vessels as well as the retinal lesions. Also, Miri and Mahloojifar [69] used the discrete curvelet transform to enhance the image ridges which, as mentioned before, play an important role in enhancing the image contrast.

Figure 2-9 provides a graphical comparison between all the aforementioned techniques of contrast enhancement (reproduced from [67] and [69]).

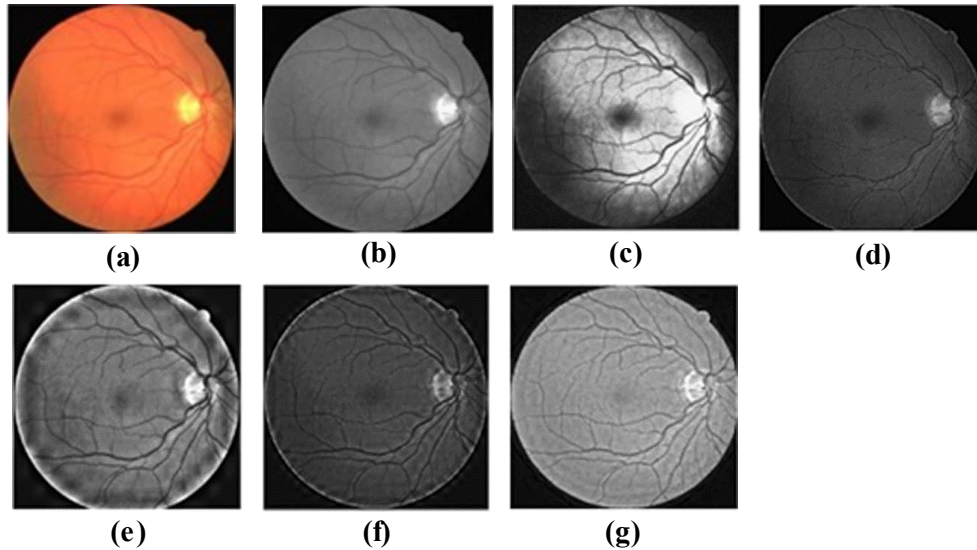


**Figure 2-9. Comparison between different techniques of contrast enhancement**

(a) Reference color image (DRIVE: 02\_test.tif)

(b) Green band of (a)

(c) Histogram equalization

(d) Unsharp masking

(e) Wavelet transform

(f) Contourlet transform

(g) Curvelet transform

### 2.3.6. Non-uniform Illumination Correction

The improper light focus of an imaging system may decrease the brightness of the retinal image around the peripheral region compared to the center of the retina, causing a non-uniform illumination referred to as vignetting, as shown by the images of Figure 2-10.

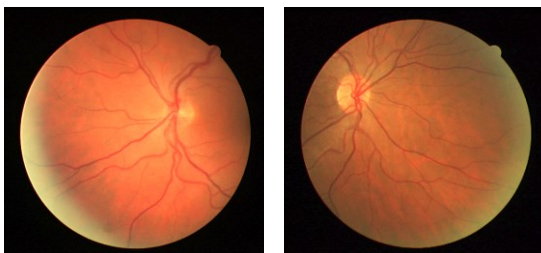


**Figure 2-10. Examples of non-uniform illumination**

Therefore, in order to overcome vignetting, Hoover and Goldbaum [41] presented an illumination equalization technique to enhance the image, in which each pixel  $I(r,c)$  in the image was corrected as follows:

$$I_{eq}(r,c) = I(r,c) + m - A(r,c) \quad \text{Equation 2-6}$$

where  $m$  is the desired average intensity (128 in an 8-bit gray-scale image) and  $A(r,c)$  is local average intensity of the pixels within a window of size  $N \times N$ . This equalization technique was also

employed by other algorithms such as [7] and [24] on the green band of the retinal images in order to adjust uneven illumination.

Using an alternative approach for equalization, Yang *et al.* [43] corrected the non-uniform illumination of an image via dividing the green band image by an over-smoothed version of it using a spatially large median filter. Figure 2-11 shows the equalized images in the green bands using the two methods (reproduced from [55]).

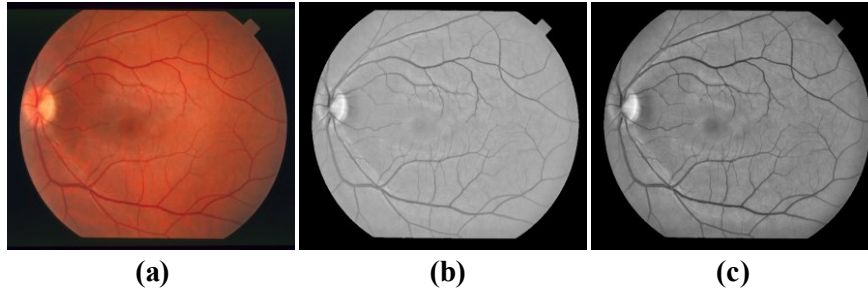


**Figure 2-11. Illumination equalization**

(a) Source image (STARE: im0255.ppm)      (b) Hoover's method      (c) Yang's method

Recently, Odstcilik *et al.* [19] preprocessed the green band of the color fundus image using a B-spline-based illumination correction method. The non-uniform illumination correction was applied together with contrast enhancement, in which a multiplicative illumination model was used to produce the corrected image  $G$ , as follows:

$$G = \frac{I}{b} - b^{max} + 128 \quad \text{Equation 2-7}$$

where the term  $I$  refers to the original intensity image and  $b$  is the background illumination model obtained by approximating the low-pass filtered image by a two-dimensional B-spline function, while the term  $(b^{max} + 128)$  ensures that the mean value of the reconstructed image will be approximately 128 (for images with 256 grey levels).

## 2.4. Landmarks Segmentation

Detecting and locating the main anatomical structures of the eye fundus, such as the optic disc, the macula, the fovea and the major blood vessels, is considered an essential step toward detecting abnormalities and analyzing lesions in the fundus images. Thus, these segmented fundus landmarks may be exploited to establish a coordinate system (retinal model) of the eye fundus which in turn may be used to determine the spatial relationship of lesions, edema and hemorrhages with reference to the optic disc and macula.

### 2.4.1. Motivation of Optic Disc Detection

Detecting the optic disc and analyzing its spatial structure serves as an indicator of various ophthalmologic pathologies such as diabetic retinopathy and glaucoma. As because of the similarity and confusion between exudates and the optic disc (Figure 2-12b), diabetic retinopathy can be diagnosed by isolating and omitting the optic disc which improves the identification of exudates, one of the main retinal abnormalities occurring in diabetic retinopathy [7], [70].

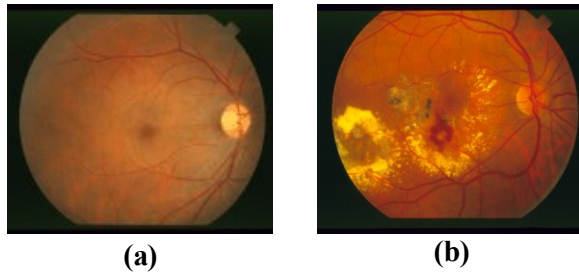


**Figure 2-12.** (a) Healthy fundus image (b) Diabetic fundus (containing exudates)

Moreover, both the cup-to-disc ratio and the ISNT rim thickness rule (Inferior > Superior > Nasal > Temporal) are two intrapapillary indicators used to diagnose glaucoma which is characterized by the cupping of the optic disc, as well as the thinning of the Inferior and Superior rims (i.e. notching), as discussed later at section 2.5.1. The pathology of glaucoma is characterized by the cupping of the optic disc which becomes ischemic due to the imbalance between the intraocular pressure and the perfusion pressure in the vessels of the retina [2], as shown in Figure 2-13.

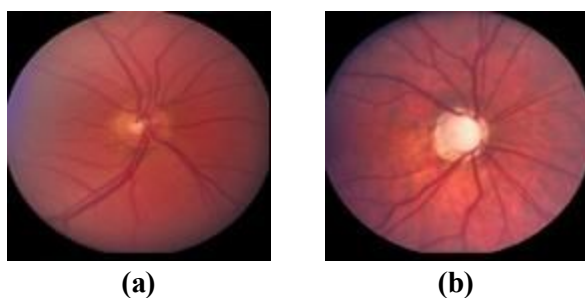


**Figure 2-13.** (a) Normal optic disc (b) Glaucomatous optic disc

### 2.4.2. Properties of the Optic Disc

The optic disc is found towards the right-hand side or the left-hand side of the fundus image for the right-eye and left-eye, respectively. It is round or vertically oval in shape, measuring about one-tenth to one-sixth the width of the image, and typically appears as a bright yellowish or white

area. Also, the optic disc appears as the convergent area of the vascular tree of blood vessels [71], [7], [61], [72], [73]. In addition, the process of locating the optic cup aims only to identifying the centroid of the optic disc, whereas detecting the optic rim (neuroretinal rim) aims to identifying the boundary between the retina and the optic disc [7]. Figure 2-14 distinguishes the optic cup and the optic rim within the optic disc.

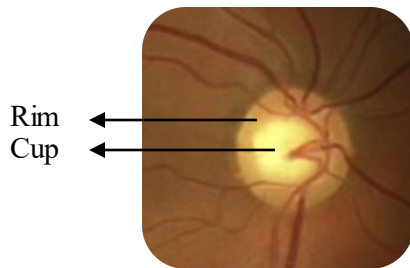


**Figure 2-14. The cup and the rim of the optic disc**

### **2.4.3. Literature of Optic Disc Segmentation**

Allam *et al.* [74] presented a full survey of optic disc segmentation algorithms through which the main methods reviewed in the literature were categorized and distinguished, as follows:

#### **i. Property-based methods**

Such techniques exploit few or all of the main characteristics of the optic disc listed in the previous section, namely its brightness, relative width, roundness, location within the fundus image, or the existence of blood vessels in its vicinity. In the early work of the optic disc detection, Goldbaum *et al.* [42] utilized most of these properties in order to jointly locate the optic disc. They combined three properties of the optic disc: the convergence of blood vessels at the optic disc, the appearance of the optic disc as a bright region, and entrance of large vessels above and below the optic disc.

Also, Sinthanayothin *et al.* [61] located the optic disc by identifying the area with the highest variation in intensity of adjacent pixels using a window whose size equal to that of the optic disc. Their approach correctly detected the optic disc with sensitivity and specificity of 99.1% on a local dataset composed of 112 TIFF fundus images.

Similarly, based on the brightness and roundness of the optic disc, Park *et al.* [75] also presented a method with a successful detection percentage of 90.25% using an approach that included thresholding, detection of object roundness, and detection of circles.

Also, Chrástek *et al.* [76] applied an averaging filter to the green-band image, and roughly located the optic disc at the point with the highest average intensity with a success rate of 97.3% on a local dataset.

Walter and Klein [77] approximated the centroid of the optic disc as the center of the largest and brightest connected object in the fundus. Their method successfully detected optic disc in all images of a local dataset composed of 30 images, and achieved a success rate of 58% on the STARE dataset.

Carmona *et al.* [18] proposed a genetic algorithm in order to obtain an ellipse that approximated the optic disc. First, they obtained a set of hypothesis points that exhibited the geometric properties and intensity levels similar to the optic disc contour pixels. The genetic algorithm was used next to find an ellipse containing the maximum number of hypothesis points in an offset of its perimeter. The results of their algorithm showed that 96% of the 110 retinal images had less than five pixels of discrepancy.

Using the Circular Hough Transform, Abdel-Ghafar *et al.* [78] were able to detect the optic disc by finding the largest circular object. Similarly, Zhu *et al.* [2], [79] also used the Hough Transform to detect the circles in which the best-fitting circle for the optic disc was chosen by using a method of intensity-based selection. They achieved a successful detection rate of 90% on the DRIVE dataset and 44.4% on the STARE dataset.

A circular transformation was designed by Lu [36] to capture both the circular shape of the optic disc as well as the image variation across the optic disc boundary, simultaneously. The variation of each pixel within the retinal image was measured along multiple evenly-oriented radial line segments of specific length. The pixels with the maximum variation along all radial line segments were determined, which were then exploited to locate both the center and the boundary of the optic disc. Experimental results showed that the center of the optic disc was accurately detected in 99.75%, 97.5%, and 98.77% of the STARE, ARIA and MESSIDOR datasets, respectively. Also, the boundary of the optic disc was accurately segmented in 93.4% and 91.7% of the STARE dataset and the ARIA dataset, respectively.

Zubair *et al.* [80] detected the optic disc by increasing its contrast using preprocessing techniques such as CLAHE, contrast stretching transformation, and extended minima transformation. Using the contrasted image, the optic disc was localized by using morphological erosion and dilation in order to remove all non-optic disc regions that are not of the size of the

optic disc. Finally, after taking negative of the image, the resultant image obtained was subtracted from the resized green-channel component to get an optic disc free image, with an accuracy of 98.65% on the MESSIDOR dataset.

Yu and Yu [81] localized the optic disc via a technique of detecting the brightest pixels iteratively, as to be robust against the existence of any bright lesions such as hard exudates. They also set thresholds for the area of the optic disc and its circularity in order to select the optic disc over other nominees. They reported that their approach achieved a detection rate of 95%, although only 40 “selected-images” of the STARE dataset were tested, which means that this rate might have been degraded if the whole dataset had been used.

As a concluding observation, it was obvious that all the aforementioned property-based methods achieved good results in normal fundus images that contained no abnormalities, but most of these approaches usually failed to detect the optic disc in pathological images where abnormalities, such as large exudates, were been confused with the optic disc due to their similar appearance.

## **ii. Convergence of blood vessels**

Instead of relying on the properties of the optic disc, an alternative approach to detect the optic disc is to exploit the information provided by the vascular tree of the retina, since the optic disc is considered as the convergence point of the few major blood vessels that split into many smaller vessels throughout the retina [7].

Taking advantage of this spatial relationship between the optic disc and blood vessels, Hoover and Goldbaum [41] developed a voting-type algorithm called fuzzy convergence in order to detect the origination of the blood-vessel network (i.e. convergence point) which was considered as the center of the optic disc in a fundus image. The input to their algorithm was a binary segmentation of the blood vessels, in which each vessel was modeled by a fuzzy segment that contributed to a cumulative voting image. The output of the algorithm was a convergence image which was thresholded to identify the strongest point(s) of convergence. This technique successfully detected 89% of the normal and abnormal images in the STARE dataset.

The Hough Transform was utilized by ter Haar [24] in two different ways. In the first method, the Hough Transform was applied only to the pixels on or close to the binary image of the retinal vasculature obtained by [12], in which the binary image was dilated on order to increase the number of optic disc candidates. This approach achieved a success rate of 96.3% on a local dataset

and 71.6% on the STARE dataset. In the second alternative method, the Hough Transform was applied only to the brightest 0.35% of the fuzzy convergence image produced by Hoover and Goldbaum [41], in which dilation was applied again to the convergence image to fill the gaps created by small vessels. This approach achieved a success rate of 97.4% on a local dataset and 65.4% on the STARE dataset.

Fleming *et al.* [82] detected the approximate region of the optic disc using an elliptical shape of the major retinal vessels which was formed using the Generalized Hough Transform. The approximate location of the optic disc was then refined via the Circular Hough Transform achieving a success rate of 98.4% of the 1056 retinal images, in which the positional accuracy was better than 50% of the diameter of the optic disc.

Ying *et al.* [83] proposed an algorithm that differentiates the optic disc from other bright regions such as hard exudates, in which the optic disc was detected based on its high fractal dimension of the converging pattern of blood vessels. With its location known, the optic disc was correctly segmented via local histogram analysis in 97.5% of the images of the DRIVE dataset.

Based on tensor voting for analyzing vessel structures, Park *et al.* [63] proposed a method to identify the location of the optic disc. The vessel patterns were first extracted by tensor voting in equalized images, and then the position of the optic disc was identified by mode detection which was based on mean-shift procedure. Their approach was tested with 90 images from the STARE dataset, which achieved 100% success rate on 40 normal images and 84% on pathological images.

In the work of Rangayyan *et al.* [2], [84], the blood vessels were first detected using Gabor filters, and then phase portrait modeling was applied to detect the convergence points of the vessels, in which the best-fitting circle for the optic disc was chosen by using an intensity-based condition. This approach achieved success rates of 100% and 69.1% for the DRIVE and STARE datasets, respectively.

### **iii. Model-based methods (template-matching)**

This type of methods is based on comparing a template image (model) with a set of candidates in order to determine the best-matching candidate. Lalonde *et al.* [35] implemented a Hausdorff-based template matching technique using edge maps, guided by pyramidal decomposition for large-scale object tracking where small bright lesions (e.g. exudates) disappear, creating fewer optic disc candidates. The edge map regions were matched to a circular template with different radii using the Hausdorff distance, and the region having the largest number of overlapped

template pixels was considered the optic disc. This approach correctly detected the center of the optic disc in 93% of a dataset of 40 images.

Another model-based approach was proposed by Osareh *et al.* [85] who created a gray-level template image by averaging the optic disc region of 25 images whose colors were normalized using histogram specification. The center of the optic disc was located by using the generated template along with gray-scale morphological filtering and active-contour modeling in which the normalized correlation coefficient was used to find the most similar match between the template and all the candidate pixels, with an average accuracy of 90.32% in detecting the boundary of the optic disc of 75 images of the retina.

Also, Li and Chutatape [86] created an optic disc model (disc-space) by applying Principal Component Analysis (PCA) to a training set of 10 intensity normalized images that were manually cropped around the optic disc. The candidate regions with the highest 1% gray-level were selected and matched to the disc-space, in which the optic disc was successfully detected in 99% of the images as the region with the smallest Euclidean distance to its projection onto the disc-space.

Also, the method proposed by Foracchia *et al.* [87] for detecting the optic disc was based on a preliminary detection of the major retinal vessels. They proposed a geometrical model to describe the general direction of retinal vessels at any given position using the coordinates of the optic disc center which were two model parameters estimated by the means of a simulated annealing optimization technique. The position of the optic disc was correctly located in 97.53% of the STARE images using the common vertex of the two model parameters (i.e. the convergence point for the blood vessels).

Lowell *et al.* [14] designed a detection filter (i.e. template) for the optic disc which was composed of a Laplacian of Gaussian filter with a vertical channel carved out of the middle corresponding to the major blood vessels exiting the optic disc vertically. This template was then correlated to the intensity component of the fundus image using full Pearson-R correlation. The optic disc was successfully detected in 99% of the images in a local dataset.

A method presented by ter Haar [24] was based on fitting the vascular orientations on a directional model (DM), using a training set of 80 images of vessel segmentations. For all the pixels in each vessels image, the orientation was calculated to form a directional vessel map, in which the DM was created by averaging, at each pixel, all the corresponding orientation values in the directional maps. At the end, each pixel in an input vasculature was aligned to the center of the

optic disc, and the pixel having the minimal distance to both DMs was selected as the optic disc location. This method detected the optic disc successfully in 99.5% of the images in a local dataset and 93.8% of the STARE dataset.

Closely related, Youssif *et al.* [7] proposed another model-based approach by matching the expected directional pattern of the retinal blood vessels found in the vicinity of the optic disc. They obtained a vessels direction map of the retinal vessels that were segmented using 2D Gaussian matched filter. The minimum difference between the matched filter and the vessels directions at the surrounding area of each of the optic disc candidates achieved a successful detection rate of 100% on the DRIVE dataset and 98.77% on the STARE dataset.

Niemeijer *et al.* [44] formulated the problem of finding a certain position in a retinal image as a regression problem. A k-nearest neighbor classifier (k-NN) was trained to predict the distance to the optic disc given a set of measurements of the retinal vasculature obtained around a circular template placed at a certain location in the image. The method was trained with 500 images for which the location of the optic disc was known, where the point with the lowest predicted distance to the optic disc was selected as the optic disc center. This supervised method was tested using 600 images of which 100 images contained gross abnormalities, and successfully located the optic disc in 99.4% of the normal images and 93% of the pathological images.

Aquino *et al.* [37] presented a template-based methodology that used morphological and edge detection techniques followed by the Circular Hough Transform to obtain an approximate circular optic disc boundary. Their methodology required an initial pixel located within the optic disc, and for this purpose, a location procedure based on a voting-type algorithm was utilized and succeeded in 99% of the cases. The algorithms were evaluated on the 1200 images of the MESSIDOR dataset, achieving a success rate of 86%.

Lu [88] used another technique for the detection of the optic disc in a way different than the one he used in [36] (previously reviewed in the *property-based methods*). In the proposed technique, the retinal background surface was first estimated through an iterative smoothing procedure. Afterwards, multiple optic disc candidates were detected through the difference between the retinal image and the estimated retinal background surface. Finally, the real optic disc was selected through the combination of the difference image and the directional retinal blood vessel which was based on the observation that the retinal blood vessels were mostly oriented vertically as they exit the optic disc. The proposed technique was evaluated over four datasets

DIARETDB0, DIARETDB1, DRIVE and STARE giving an accuracy of 98.88%, 99.23%, 97.50% and 95.06%, respectively.

Instead of creating an image and using it as a template, Deghani *et al.* [72] constructed three histograms as a template for localizing the center of the optic disc using four retinal images from the DRIVE dataset, in which each histogram represented one color channel. Then, an 80×80 window was moved through the retinal image to obtain the histogram of each channel. Finally, they calculated the correlation between the histogram of each channel in the moving window and the histograms of its corresponding channel in the template. The DRIVE, STARE, and a local dataset composed of 273 images were used to evaluate their proposed algorithm, in which the success rate was 100%, 91.36% and 98.9%, respectively.

Zhang and Zhao [89] proposed a method for detecting the optic disc accurately in an efficient way. First, the algorithm identified a number of possible vertical windows (x-coordinates) for the optic disc according to three characteristics of retinal vessels, which are: (1) the high density of vessels at optic disc vicinity, (2) compactness of the vertical vascular segments around the optic disc center, and (3) the uniform distribution of vessels. Consequently, the y-coordinate of the optic disc is identified according to the vessels direction via parabola curve fitting using the General Hough Transform. The proposed method was tested on four datasets: DIARETDB0, DIARETDB1, DRIVE and STARE, in which the optic disc was correctly detected in all images of each dataset, except only one image in the STARE dataset.

Table 2-2 chronologically summarizes the aforementioned methods of optic disc localization.

**Table 2-2. List of optic disc detection methods**

	Approach	Dataset	SENS	ACC
1	Goldbaum et al., 1996 [42]: vessels convergence, OD brightness, and large vessels entrance	None	-	-
2	Sinthanayothin et al., 1999 [61]: High intensity variation	Local dataset (112 images) STARE (81 images) <sup>1</sup>	0.9911 0.4200	- -
3	Lalonde et al., 2001 [35]: Hausdorff template matching & pyramidal decomposition	Local dataset (40 images) STARE (81 images) <sup>1</sup>	1.0000 0.7160	0.9300 -
4	Walter & Klein, 2001 [77]: Largest brightest connected object	Local dataset (30 images) STARE (81 images) <sup>1</sup>	0.9000 0.5802	- -
5	Chrástek et al., 2002 [76]: Highest average intensity	Local dataset (261 images)	0.9732	0.8171

<sup>1</sup> Additional results for the STARE dataset were obtained from the comparative study done by ter Haar, 2005.

	<b>Approach</b>	<b>Dataset</b>	<b>SENS</b>	<b>ACC</b>
6	Osareh et al., 2002 [85]: Averaged OD-images template matching	Local dataset (75 images) STARE (81 images) <sup>1</sup>	0.9032 0.5800	- -
7	Hoover & Goldbaum, 2003 [41]: Fuzzy convergence of blood vessels	STARE (81 images)	0.8888	-
8	Foracchia et al., 2004 [87]: Geometrical model of vessel structure	STARE (81 images)	0.9753	-
9	Li & Chutatape, 2004 [86]: Template matching via Principal Component Analysis	Local dataset (89 images)	0.9888	0.9400
10	Lowell et al., 2004 [14]: Laplacian of Gaussian template & full Pearson-R correlation	Local dataset (90 images)	0.9889	-
11	ter Haar, 2005 [24]: Hough Transform applied to the pixels close to the retinal vasculature	STARE (81 images) Local dataset (191 images)	0.7160 0.9634	- -
12	ter Haar, 2005 [24]: Hough Transform applied to the fuzzy convergence image	STARE (81 images) Local dataset (191 images)	0.6543 0.9738	- -
13	ter Haar, 2005 [24]: Fitting the vasculature orientations on a directional model	STARE (81 images) Local dataset (191 images)	0.9948 0.9383	- -
14	Park et al., 2006 [75]: Brightness and roundness detection	DRIVE (40 images)	0.9025	-
15	Abdel-Ghafar & Morris, 2007 [78]: Circular Hough Transform	None	-	-
16	Fleming et al., 2007 [82]: Elliptical form of blood vessels	Local dataset (1056 images)	0.9840	-
17	Park et al., 2007 [63]: Tensor voting and adaptive mean-shift	STARE (90 images)	0.8444	-
18	Ying et al., 2007 [83]: Fractal dimension of blood vessels and local histogram analysis	DRIVE (40 images)	0.9750	-
19	Carmona et al., 2008 [18]: Approximating elliptical form of optic disc via genetic algorithm	Local dataset (110 images)	0.9636	-
20	Youssif et al., 2008 [7]: Vessels' direction matched filter	DRIVE (40 images) STARE (81 images)	1.0000 0.9877	- -
21	Niemeijer et al., 2009 [44]: Vasculature measurements and the k-NN regression	Local dataset (600 images)	0.9300	-
22	Aquino, et al., 2010 [37]: Morphology, edge detection and circular Hough transform	MESSIDOR (1200 images)	0.8600	-
23	Lu, 2010 [88]: Estimation of retinal background surface and directional blood vessel information	DIARETDB0 (130 images) DIARETDB1 (89 images) DRIVE (40 images) STARE (81 images)	0.9888 0.9923 0.9750 0.9506	- - - -

	Approach	Dataset	SENS	ACC
24	Rangayyan et al., 2010 [84]: vessels convergence by Gabor filters and phase portrait modeling	DRIVE (40 images)	1.0000	-
		STARE (81 images)	0.6913	-
25	Zhu et al., 2010 [79]: Circle detection via Hough transform	DRIVE (40 images)	0.9000	-
		STARE (81 images)	0.4444	-
26	Lu, 2011 [36]: Circular transformation and image variation along multiple radial line segments	ARIA (120 images)	0.9750	0.9170
		MESSIDOR (1200 images)	0.9975	-
		STARE (81 images)	0.9876	0.9340
27	Dehghani et al., 2012 [72]: Histogram-based template matching	DRIVE (40 images)	1.0000	-
		Local dataset (273 images)	0.9890	-
		STARE (81 images)	0.9136	-
28	Zubair et al., 2013 [80]: Contrast enhancement and morphological transformation	MESSIDOR (1200 images)	1.0000	0.9865
29	Yu & Yu, 2014 [81]: Iterative brightest pixels extraction	STARE subset (40 images)	0.9500	-
30	Zhang & Zhao, 2014 [89]: Vessels distribution and directional characteristics	DIARETDB0 (130 images)	1.0000	-
		DIARETDB1 (89 images)	1.0000	-
		DRIVE (40 images)	1.0000	-
		STARE (81 images)	0.9877	-

According to the previous table, the plots for the sensitivity of detecting the optic disc are illustrated in Figure 2-15, Figure 2-16 and Figure 2-17, for the reviewed algorithms over the DRIVE, STARE and other miscellaneous datasets, respectively.

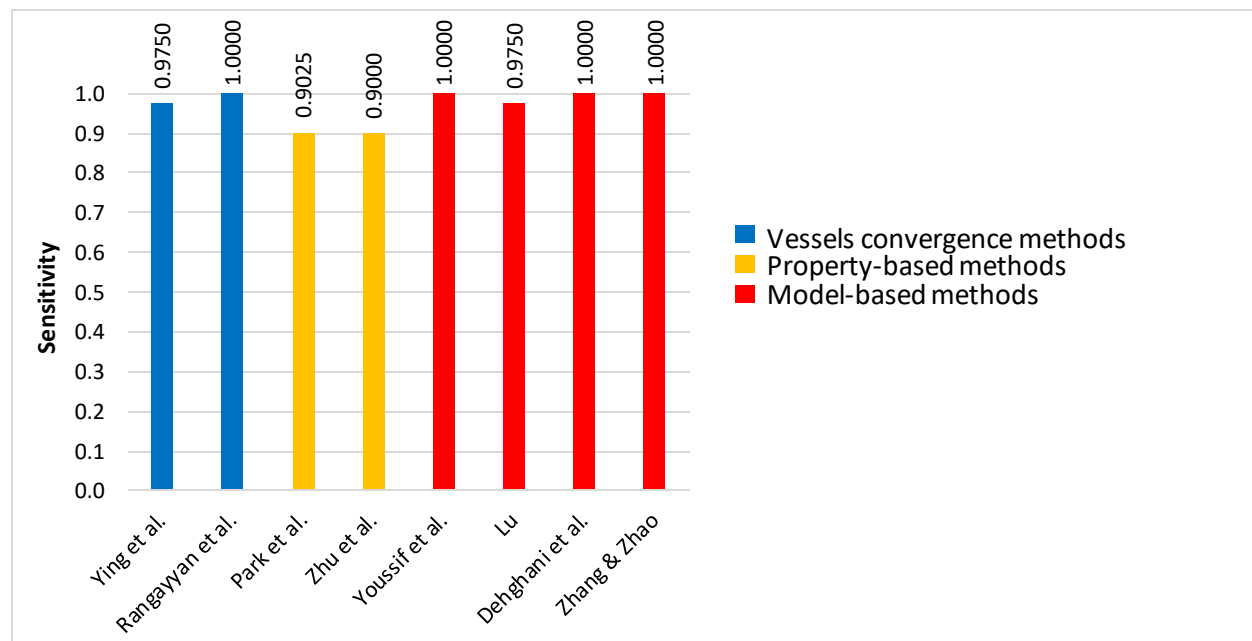


Figure 2-15. Sensitivity of OD detection algorithms over the DRIVE dataset

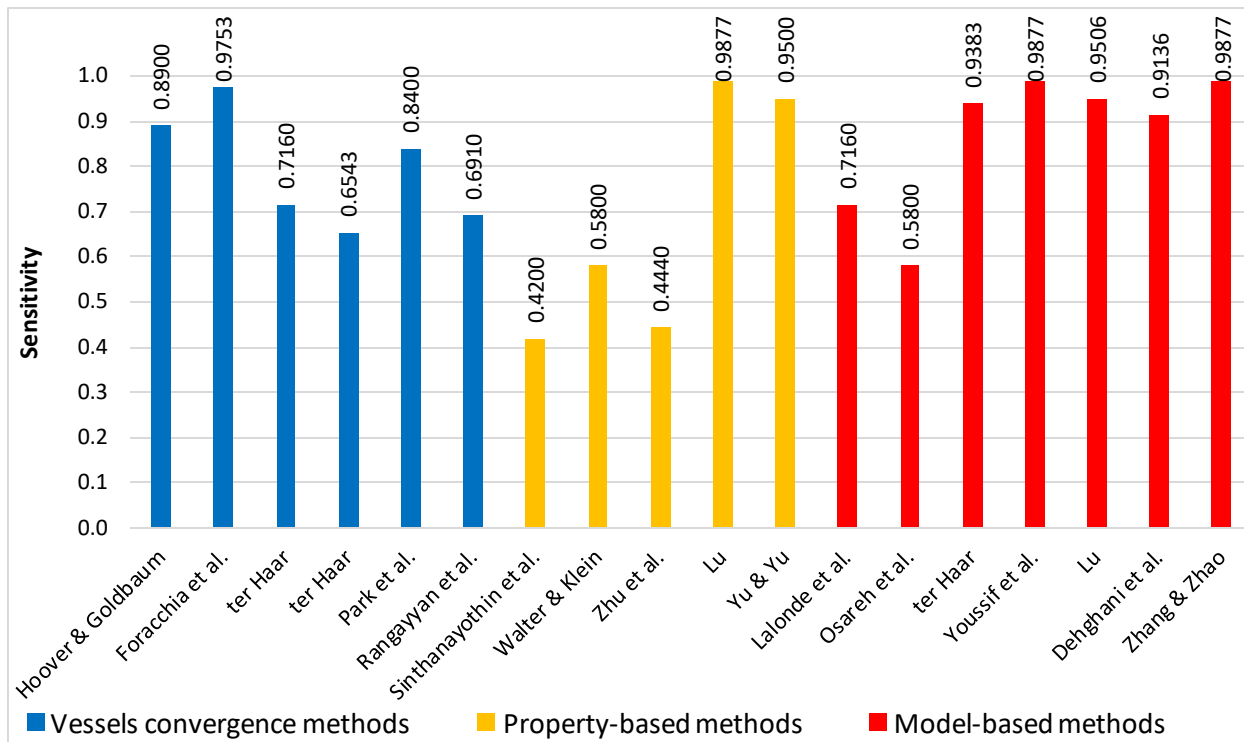


Figure 2-16. Sensitivity of OD detection algorithms over the STARE dataset

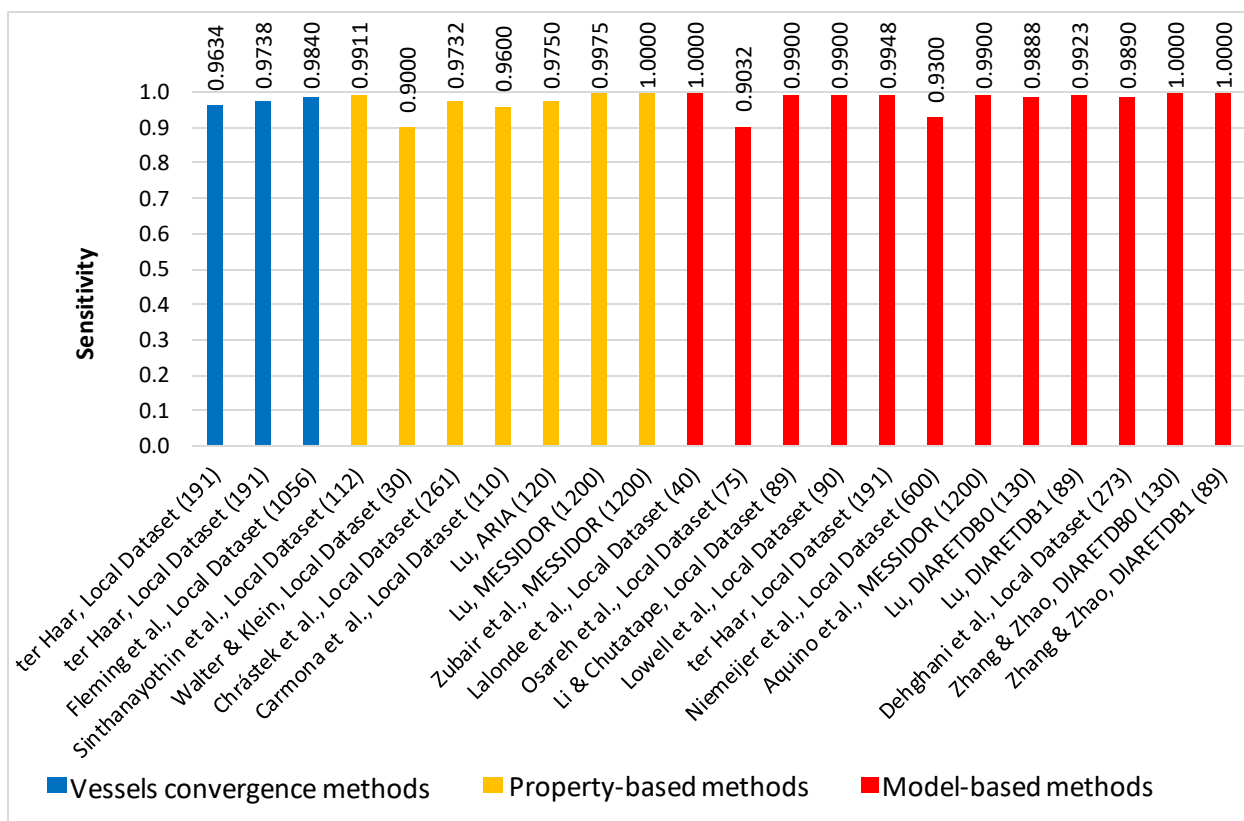


Figure 2-17. Sensitivity of OD detection algorithms over miscellaneous datasets

## **2.5. Detection of Abnormalities**

The detection of lesions occurring in the eye fundus, such as microaneurysms, exudates, hemorrhages, neovascularization and optic disc abnormalities, can assist in the diagnosis and treatment of serious ophthalmological diseases such as glaucoma, diabetic retinopathy, and age-related macular degeneration. At August 2014, the World Health Organization (WHO) reported that 285 million people were estimated to be visually impaired worldwide: 39 million were blind and 246 had low vision, in which 80% of all visual impairment could be prevented or cured. Moreover, around 90% of the world's visually impaired people lived in low-income settings [90].

The following subsections describe the motivations, clinical indicators, and the literature for two of the most leading causes of visual impairment and blindness: glaucoma and diabetic retinopathy.

### **2.5.1. Motivation of Detecting Glaucoma and Diabetic Retinopathy**

Statistically, about 60 million people all over the world were found to have glaucoma in 2010 who were estimated reach 80 million by 2020 [91], and according to the Egyptian Society for the Glaucomas (ESG), about 0.5% to 1% of the population in Egypt suffer from glaucoma (i.e. more than half a million people) [92]. However, glaucoma presents a great health motivation over other eye diseases, such as cataract and diabetic retinopathy, because the damage that glaucoma causes is permanent and irreversible (i.e. could not be cured). Moreover, glaucoma patients lose their vision gradually such that they are often unaware of it until their sight has already been compromised. For this reason, glaucoma is often called the "sneak thief of sight" [93].

Besides glaucoma, diabetic retinopathy is another sight-threatening complication caused by diabetes mellitus affecting the retina, in addition to the kidneys (diabetic nephropathy) and the nervous system (diabetic neuropathy) [9], [17]. Thus, diabetic retinopathy is a main cause of blindness occurring as a result of long-term accumulated damage to the small blood vessels in the retina. As published by the WHO at June 2016 [94], 2.6% of global blindness could be attributed to diabetic retinopathy, in which the number of people with diabetes had risen from 108 million in 1980 to 422 million in 2014. Moreover, the global prevalence of diabetes among adults over 18 years of age had risen from 4.7% in 1980 to 8.5% in 2014. Accordingly, the greatest emphasis in automated diagnosis had unsurprisingly been given to the detection of diabetic retinopathy.

## 2.5.2. Clinical Indicators of Glaucoma

Glaucoma is a neuropathy disease that occurs due to the damage and loss of ganglion cells. Typically, there are five main different types of glaucoma: primary open-angle, normal-tension, closed-angle, congenital, and secondary glaucoma [93]. Glaucomatous damage typically affects the intrapapillary region (i.e. the optic disc itself), as well as the peripapillary region which surrounds the optic disc. Thereby, ophthalmologists agreed that glaucoma can be diagnosed through the following five indicators within the intrapapillary and peripapillary regions [74], [94]:

### (i) Cup-to-Disc Ratio (CDR)

The CDR is defined as the ratio of the vertical diameter of the optic cup to the vertical diameter of the neuroretinal rim which is an important structural indicator for assessing the presence of glaucoma characterized by the cupping of the optic disc, as shown earlier in Figure 2-13. Clinically, glaucoma is suspicious with a CDR more than 0.6. However, the CDR in only one eye is not always a reliable indicator due to the varying cup size among patients. Therefore, a glaucomatous optic cup can be identified more precisely via the cupping asymmetry in the left-and-right eye pair, where the asymmetry ratio is typically more than 0.2 [95], [96].

### (ii) ISNT Rule

However, it is possible to have a healthy optic disc with a large CDR (especially in myopic eyes), and it is also possible to have a glaucomatous optic disc with a normal CDR. So, besides CDR, glaucoma is also diagnosed when the optic cup is tilted (i.e. the neuroretinal rim thickness violates the ISNT rule). The normal optic disc typically demonstrates a configuration where the inferior neuroretinal rim (i.e. lower rim) is the widest portion of the rim, followed by the superior rim (i.e. upper rim), and then the nasal rim (i.e. inner, nearest the nose), and finally the temporal rim (outer, nearest the temple) which is the narrowest [97], [98], [99], as shown in Figure 2-18.

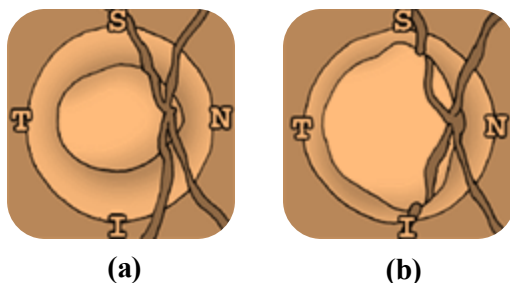


**Figure 2-18. Sketch of the ISNT rule for the thickness of the neuroretinal rim**

**(a)** Healthy neuroretinal rim – follows the ISNT configuration

**(b)** Glaucomatous neuroretinal rim – violates the ISNT configuration

### (iii) Disc Hemorrhages

Another important clinical indicator of glaucoma is the presence of splinter-like hemorrhages within the optic disc whose existence is more common in normal-tension glaucoma, compared to all other types of glaucoma. Moreover, disc hemorrhaging most often occurs in the same areas of, and also associated with, rim notching and NFLD (i.e. within the inferior-temporal and superior-temporal regions). Besides, disc hemorrhages may repeatedly appear and disappear at different intervals of time, and accordingly, the color of disc hemorrhages depends upon how long they have been present, since they are transient, lasting from two to six months [94], [100]. Figure 2-19 shows different examples of optic disc hemorrhages which have many appearances, depending on how long they have been present.

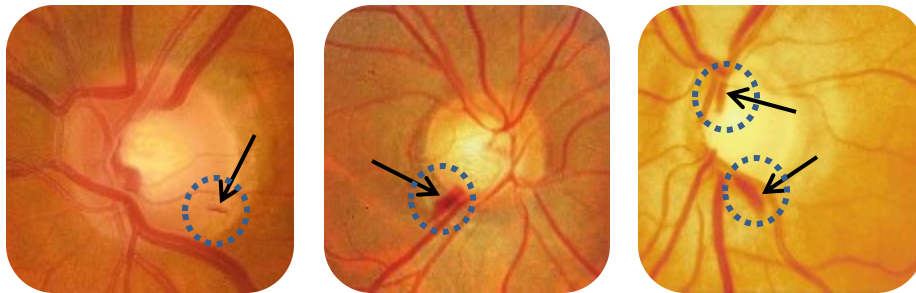


**Figure 2-19. Optic disc splinter hemorrhages**

### (iv) Nerve Fiber Layer Defect (NFLD)

The retinal nerve fiber layer (RNFL) is formed by the ganglion cell axons which represents the innermost layer of the eye fundus. Due to the loss of ganglion cells in glaucoma, it is well known that the NFLD precedes and subsequently leads to the enlargement of the optic cup; and hence the NFLD is considered one of the earliest signs of glaucoma [101].

The RNFL is best observed using red-free or green light images where the normal healthy eye has a thick layer of retinal nerve fibers which can be seen as fine bright striations (strips). The RNFL demonstrates a “bright-dark-bright” pattern when viewed up from the superior-temporal region down to the inferior-temporal region. In other words, the retina shines in the regions in which the RNFL is thickest (i.e. superior-temporal and inferior-temporal regions), whereas the area between the disc and the macula (i.e. temporal region) appears darker [94], [95], [102]. Figure 2-20(a) shows an example of the bright striations around the superior and inferior parts in a healthy retina creating the bright-dark-bright pattern (reproduced from [102]).

On the other hand, the region around the optic disc with NFLD gets darker and changes from stripy-texture to wedge-shaped form. Also, blood vessels appear darker with sharp reflexes in the region of NFLD, as shown in Figure 2-20 (b) [102].

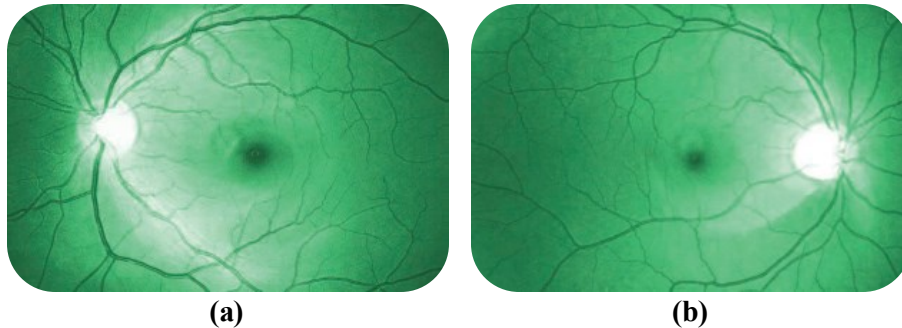


**Figure 2-20. Red-free optic disc image showing nerve fiber layer**

**(a)** Normal NFL: bright-dark-bright strip pattern **(b)** NFLD below the optic disc

There are two kinds of NFLD, namely, localized and diffuse. The localized NFLD appears as a wedge-shaped dark area that follows the pattern of the RNFL originating from the optic disc [94], [95]. In such defects, the specificity is very high but the sensitivity is low since these defects are a definite sign of pathology, but can occur in diseases other than glaucoma [95]. Figure 2-21 shows an example of a localized NFLD showing a dark wedge-shaped defect that touches the edge of the optic disc and increases in width toward the periphery.

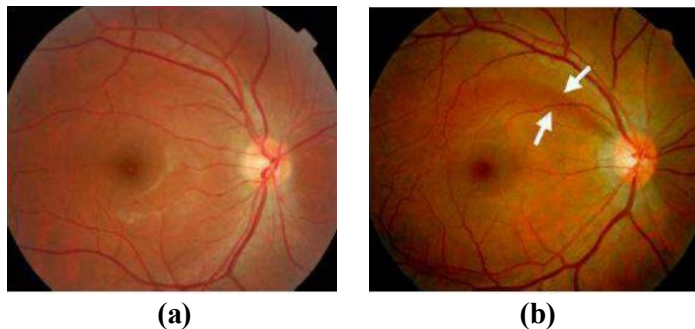


**Figure 2-21. Example of localized NFLD**

**(a)** Normal NFL **(b)** Localized NFLD with a dark wedge

On the other hand, diffuse NFLD can be seen in advanced glaucoma. It is usually more difficult to be detected in one eye, but it is easily recognized when both eyes are compared together. In diffuse NFLD, there is a general reduction of the RNFL brightness causing the normal “bright-dark-bright” pattern to be lost and look like a “dark-dark-dark” pattern (i.e. appears completely dark) [94], [95], [102].

### (v) Peripapillary Atrophy (PPA)

The peripapillary region, as its name implies, is the area located around the periphery of the papilla (i.e. just outside the optic disc). Thus, the peripapillary atrophy (PPA) refers to the thinning and degeneration of the chorioretinal tissue around the optic disc. Two distinct zones of atrophy, Alpha zone ( $\alpha$ ) and Beta zone ( $\beta$ ) can surround the optic disc, where the Alpha zone is located on the outer periphery of the Beta zone, as shown in Figure 2-22.

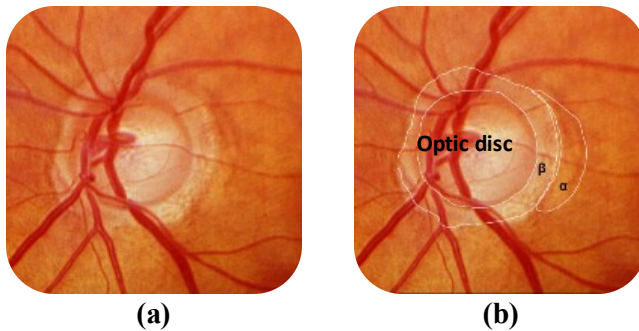


**Figure 2-22. Peripapillary atrophy**

(a) Glaucomatous papilla (b) Marked alpha and beta zones

The outer zone alpha ( $\alpha$ ) is present in almost any eye (i.e. normal and glaucomatous). This zone is characterized by a region of irregular hypopigmentation and hyperpigmentation of the retinal pigment epithelium (RPE). The inner beta zone ( $\beta$ ) is more often observed in glaucomatous eyes than in healthy eyes, which is characterized by visible sclera and visible large choroidal vessels, located between the peripapillary ring and alpha zone, showing a complete loss of the RPE. The peripapillary atrophy is located and associated within the region of neuroretinal rim loss, with the atrophy being largest in the corresponding area of thinner neuroretinal rim [94], [103].

Table 2-3 summarizes the main structural indicators described within this section as well as the functional characteristics indicating the presence or the suspect of glaucoma.

**Table 2-3. Glaucoma structural and functional indicators**

Clinical Indicator	Glaucoma Risk Reference	Viewable in fundus image
Cup-to-disc ratio (CDR)	Greater than 0.6	✓
Left-Right cup asymmetry	Greater than 0.2	✓
ISNT irregularity	Thinning of inferior & superior rim (notching)	✓
Disc hemorrhages	Present at inferior & superior sectors	✓
Nerve fiber layer defects	Present	✓
Peripapillary atrophy	Beta zone appears adjacent to rim loss region	✓

Rim color	Pink (except in very end-stage disease)	✓
Intraocular pressure (IOP)	Higher than 21 mmHg	×
Defect of visual field (VF)	Present	×
Myopia (near sightedness)	Present	×
Age	Above 60 years	×
Ethnicity	African / Hispanic / East Asian	×
Family history	Positive	×

### 2.5.3. Clinical Indicators of Diabetic Retinopathy

There are no significant symptoms in the early stages of diabetic retinopathy, but the severity of diabetic retinopathy increases during the time. Thereby, diabetic retinopathy can be classified into four levels according to the grade of severity: (1) mild non-proliferative diabetic retinopathy (NPDR), (2) moderate NPDR, (3) severe NPDR, and (4) proliferative diabetic retinopathy (PDR) [17], [104], [105].

Moreover, the indicators of diabetic retinopathy can be roughly categorized into two sets: “dark lesions” which include microaneurysms and hemorrhages, and “bright lesions” which include hard and soft exudates [56]. Specifically, the mild NPDR typically begins as small changes in the retinal vessels, where the first detectable abnormality is the microaneurysms which are local distensions of the retinal vessels. Microaneurysms eventually rupture to form hemorrhages deep within the retina, which because of their dot-like appearance, they are called “dot-and-blot” hemorrhages. Over time, retinal edema and hard exudates are followed by the increased permeability of the vessels’ walls. The hard exudates are lipid formations leaking from these weak blood vessels. This state of the retinopathy is called moderate NPDR. However, if the aforementioned abnormalities appear in the central vision area (i.e. macula), it is called diabetic maculopathy. As this state of NPDR progresses, the blood vessels become obstructed resulting in white fluffy patches in the retina called cotton wool spots or soft exudates. When a significant number of hemorrhages, soft exudates, or vascular abnormalities are encountered, the state of the retinopathy is graded as severe NPDR. This severe NPDR can quickly turn into proliferative diabetic retinopathy (PDR) when extensive lack of oxygen causes the development of new fragile vessels (i.e. neovascularization) which is a serious sight-threatening state. The proliferative diabetic retinopathy may cause sudden loss in visual acuity or, in worst case, permanent blindness due to vitreous hemorrhage or detachment of the central retina [17], [105]. Figure 2-23 illustrates all these different types of the “dark” and “bright” abnormalities occurring in diabetic retinopathy.



**Figure 2-23. Abnormalities occurring in eye fundus due to diabetic retinopathy**

Table 2-4, as proposed by Wilkinson *et al.* [105], provides a severity grading scale for the different levels of diabetic retinopathy according to the abnormalities observed within the retina.

**Table 2-4. International clinical diabetic retinopathy disease severity scale**

Severity Level of Diabetic Retinopathy	Observable Abnormalities
Mild NPDR	Microaneurysms only.
Moderate NPDR	Microaneurysms and/or soft exudates but less than "Severe NPDR".
Severe NPDR	Any of the following and no signs of PDR: 1. More than 20 intraretinal hemorrhages in each of four quadrants. 2. Definite venous beading in two or more quadrants. 3. Prominent intraretinal microvascular abnormalities in one or more quadrants.
Proliferative DR	One or more of the following: 1. Definite neovascularization 2. Vitreous/pre-retinal hemorrhage

#### 2.5.4. Literature of Glaucoma Diagnosis

Fundus images were, and are still, widely used by many ophthalmologists for diagnosing glaucoma instantly and spontaneously, which makes them suitable for large-scale screening. This is because of their fast and low-cost acquisition compared to images captured via other imaging modalities reviewed in section 1.1.2, such as OCT and HRT. Thus, most of the work done for diagnosing glaucoma typically exploited one or more of the main structural characteristics of glaucomatous optic disc described in section 2.5.2. Moreover, some other very few approaches also employed some of the functional features of glaucomatous subjects, such as the visual field defect, myopia and the high intraocular pressure. These functional features are considered an additional source for diagnosing glaucoma, but obviously can never be viewed within the captured fundus images, as shown before in Table 2-3.

For instance, Song *et al.* [106] utilized a set of fuzzy “if-then” rules that defined a set of criteria for glaucoma diagnosis. That set of diagnosis criteria was based on two structural features of the optic disc which were the NFLD and CDR. Moreover, in order to increase the accuracy of glaucoma diagnosis, the fuzzy set also used two more functional features of the eye which were the visual field test and the intraocular pressure measurement. Using 128 photographs, the authors claimed that their fuzzy set technique obtained sufficient sensitivity and specificity, without reporting quantitative results.

Hayashi *et al.* [107] relied on the detection of NFLD in the fundus images in order to diagnose glaucoma. At the beginning, the blood vessels were removed from the original image using morphological operations. Consequently, the optic disc was detected within the vessels-free image using snakes, which was then transformed into a rectangular array using a polar coordinate read-out. The NFLD regions were finally localized as vertical dark bands by using Gabor filtering. Their proposed technique detected 71% of the NFLD regions within 52 fundus images with an average of 3.2 false positives per image.

Continuing their previous work described in the preceding paragraph, Muramatsu *et al.* [101] again relied on the detection of NFLD for early diagnosis of glaucoma. Similar to their previous work, the major blood vessels were first removed from the fundus image. Afterwards, the images were transformed by creating a set of elliptical curves that represented the estimated paths of the retinal nerves. Consequently, Gabor filtering was applied in order to enhance the contrast of NFLDs, in which the band-like regions darker than the surrounding pixels were selected as NFLD

candidates. For each of these initial candidates, six features were used by a neural network to determine the likelihood score of being a true NFLD.

Muramatsu *et al.* [108] again extended their previous work by presenting a technique for detecting the peripapillary atrophy (PPA) which is the other peripapillary feature of glaucoma. The objective of their procedure was to detect the PPA by using a texture analysis based on the gray-level co-occurrence matrix. In a dataset of 26 images, the sensitivity and specificity for detecting moderate-to-severe PPA regions was 73% and 95%, respectively.

Liu *et al.* [109] proposed ARGALI system which automatically measured the CDR for the sake of automated glaucoma risk assessment. They used the variational level-set algorithm to extract and segment the optic disc. Subsequently, the optic cup was segmented using a multi-modal approach in which a color histogram analysis was first performed; afterwards the optic cup boundary was segmented by applying the level-set algorithms, and finally the segmented cup was smoothed using ellipse fitting. At the last stage of ARGALI, a multi-layer neural network was proposed in order to fuse the results obtained via the various modes.

In the same direction, Burana-Anusorn *et al.* [110] presented a technique for measuring the CDR automatically in order to detect glaucoma. For extracting the optic disc, they exploited two methods: Canny edge detection method as well as a variational level-set method. As for the optic cup, it was extracted using color component analysis and threshold level-set method. At the end, ellipse fitting was applied in order to reshape the boundaries of the extracted disc and cup. In a dataset of 44 images, their approach showed that the sensitivity of glaucoma classification was 80%, and the specificity was 93%.

Nayak *et al.* [111] extracted three intrapapillary features for automated glaucoma diagnosis which were CDR, size of optic disc, ISNT ratio. The optic disc and the optic cup were segmented via the red and green planes, respectively, after inpainting the blood vessels using morphological operations. Those three features were used to classify the normal and glaucomatous images using a neural network classifier, achieving a sensitivity and specificity of 100% and 80%, respectively.

Joshi *et al.* [112] proposed a technique for glaucoma diagnosis via an intrapapillary indicator (i.e. CDR). They then extended their work by proposing another technique to detect the peripapillary glaucomatous features (i.e. PPA and NFLD) [113]. In their former work [112], the cup boundary was detected in monocular fundus images based on the vessel-bends at the boundary of the optic cup. The bends in a vessel were robustly detected using a region of support concept.

Consequently, a reliable subset of vessels bends, called r-bends, was obtained using a multi-stage selection algorithm, which in turn helped to detect the desired cup boundary using a local spline fitting approach. Moreover, in their latter work for detecting the PPA and NFLD indicators [113], they proposed a detection algorithm based on the salience property associated with these two indicators. They first extracted candidate regions of interest along with the respective adjacent region. Then, they modeled the region of interest as a region that was significantly different from the adjacent image regions, at an appropriate feature level.

Based on the CDR evaluation, Madhusudhan *et al.* [114] presented and tested three different techniques for detecting glaucoma. The proposed methods were multi-thresholding, active contour model (i.e. snakes), and region-growing segmentation. The fundus images were first preprocessed via illumination correction, blood vessels removal, and optic disc normalization. Afterwards, the disc and cup were segmented and thereby the CDR ratio was measured using each of the three mentioned techniques. Their comparative analysis showed that the region-growing technique achieved the best results with sensitivity and specificity of 94.73% and 100%, respectively.

Cheng *et al.* [115] proposed a superpixel-based classification framework for the optic disc and optic cup segmentation to be used for glaucoma screening. Their approach used the simple linear iterative clustering algorithm to aggregate nearby pixels into superpixels. In order to segment the optic disc, they exploited histograms as well as center surround statistics to classify each superpixel as “disc” or “non-disc”. Along with the histograms and center surround statistics, they also included the location information in order to segment the optic cup. Finally, a support vector machine with linear kernel was applied to classify superpixels as “discs” and “non-discs”, as well as “cups” and “non-cups”. At the end, the CDR was computed for glaucoma screening in two different datasets, achieving areas under curve of 0.8 and 0.822.

Table 2-5 lists the aforementioned methods for glaucoma detection in a chronological order.

**Table 2-5. List of glaucoma detection methods**

	<b>Approach</b>	<b>Glaucoma Indicators</b>	<b>Dataset size</b>	<b>SENS</b>	<b>SPEC</b>	<b>ACC</b>
<b>1</b>	<b>Song <i>et al.</i>, (2005)</b>	CDR, NFLD, IOP, VF	128 images	-	-	-
<b>2</b>	<b>Hayashi <i>et al.</i>, (2007)</b>	NFLD	52 images	0.7100	0.9680	
<b>3</b>	<b>Liu <i>et al.</i>, (2009)</b>	CDR	23 images	0.9500		
<b>4</b>	<b>Nayak <i>et al.</i>, (2009)</b>	CDR, ISNT	61 images	1.0000	0.8000	0.9000

Approach	Glaucoma Indicators	Dataset size	SENS	SPEC	ACC	
5	Muramatsu <i>et al.</i> , (2010)	NFLD	162 images	0.9100		
6	Joshi <i>et al.</i> , (2011)	CDR	138 images			
7	Muramatsu <i>et al.</i> , (2011)	PPA	26 images	0.7300	0.9500	
8	Madhusudhan <i>et al.</i> , (2011)	CDR	25 images	0.9473	1.000	
9	Joshi <i>et al.</i> , (2012)	PPA, NFLD	139 images			
10	Burana-Anusorn <i>et al.</i> , (2013)	CDR	44 images	0.8000	0.9300	0.8900
11	Cheng <i>et al.</i> , (2013)	CDR	2326 images			

### 2.5.5. Literature of Diabetic Retinopathy Diagnosis

As mentioned previously in section 1.2.2, eye fundus abnormalities are identified either for detecting or for monitoring a disease such as diabetic retinopathy. Automatic screening systems usually approach the disease detection in a direct manner using shape, color and domain knowledge of diabetic retinopathy indicators. However, abnormalities can also be identified indirectly by identifying changes between two images of the same eye taken at different intervals of time. The direct approach contributes to detecting diabetic retinopathy, whereas the indirect approach contributes to monitoring its progress or deterioration. Moreover, most of the screening systems also aim to detect the fundus landmarks such as the optic disc, macula and blood vessels, and then eliminate them in order to facilitate the detection of abnormalities that have similar appearance in color and shape [17].

For instance, Harangi *et al.* [116] enhanced the visual appearance of the exudates by eliminating the optic disc as well as improving the contrast of the green channel via CLAHE. Then, they identified the candidate regions containing exudates via morphological closing and reconstruction. Consequently, 56 descriptors were extracted for each candidate pixel to classify them, where the most relevant features were selected to train a boosted naïve Bayes classifier. This approach achieved a sensitivity of 63% over the DIARETDB1 dataset.

Similar to the previous method of preprocessing, Jaafar *et al.* [117] first enhanced the contrast of the green channel using CLAHE. Consequently, the hard exudates were detected by top-down image segmentation in order to partition the image into two homogeneous regions followed by Canny edge detection and region growing to segment the candidates of hard exudates. These

candidates were classified into either “exudates” or “non-exudates” using a rule-based classifier. The proposed method successfully detected the hard exudates in 93.2% of the 106 images picked from the DIARETDB1 and MESSIDOR datasets.

Kumar *et al.* [118] employed histogram analysis to detect exudates. First, the contrast of the image was changed via the nonlinear curve with brightness values of the HSV space, in which gamma correction was applied on each of the red and green components of the image. Then, the exudates candidates were detected using histogram analysis. Finally, multi-channel histogram analysis was performed in order to eliminate the false positive candidates in the optic disc. This algorithm was tested over a dataset of 158 images achieving a sensitivity and specificity of 88.45% and 95.5%, respectively.

Sopharak *et al.* [119] preprocessed the image in order to enhance its contrast and eliminate the optic disc. Then, they carried out a set of experiments on feature selection and exudate pixel classification using a naïve Bayes classifier, which proved that the best feature set is a combination of six features: (1) the preprocessed pixel intensity, (2) the standard deviation of the preprocessed intensities in a window around the pixel, (3) the pixel’s hue, (4) the number of edge pixels in a window around the pixel, (5) the ratio between the size of the pixel’s intensity cluster and the optic disc, and (6) the response of the pixel to Gaussian filter derivative. Their approach correctly classified the exudates in 93.38% of a dataset containing 39 images.

Also, in order to prevent confusion with exudates, Sreng *et al.* [120] first detected and eliminated the optic disc through image binarization, ROI-based segmentation and morphological reconstruction. Then, the exudates were detected by applying the maximum entropy thresholding to filter out the bright pixels, and finally, exudates were extracted via morphological reconstruction. This exudates extraction method was tested over 100 fundus images achieving a sensitivity of 91%.

Eadgahi and Pourreza [121] detected and eliminated the blood vessels using bottom-hat transformation and then extracted the bright components of high intensities using the top-hat transformation. After extracting the bright components, their method consequently distinguished the exudates by locating and eliminating the optic disc via its distinctive properties such as its high intensity and its high density of blood vessels. Their method successfully extracted exudates with an average sensitivity of 78.28% over the DIARETDB1 dataset.

Sinthanayothin *et al.* [64] detected the exudates based on a recursive region-growing segmentation algorithm. Their approach clustered similar pixels using the intensity difference as a criterion for recursive region growing in order to define an “exudate” and “non-exudate” image. Then, a binary image was produced via thresholding in which the regions containing the exudates were overlaid onto the original image. This region-growing technique achieved a sensitivity and specificity of 88.5% and 99.7%, respectively, within a dataset composed of 30 images of which 21 contained exudates.

Li and Chutatape [86] utilized the LUV color space for segmenting exudates. The Canny edge detector was employed along with the region growing algorithm based on three thresholds, namely, the gradient of the pixel, the difference between pixel value and the region’s mean value, and the difference between pixel value and seed value. Their approach was tested on a dataset of 35 images achieving a sensitivity and specificity of 100% and 71%, respectively.

Osareh *et al.* [122] normalized the fundus images via histogram specification, and then applied local contrast enhancement on the intensity channel “I” of the HSI color space. Afterwards, they detected the coarse hard exudates regions using fuzzy C-means clustering with Gaussian smoothed histograms for each color channel in the fundus image. In order to classify the segmented regions into exudates and non-exudates, an artificial neural network classifier was employed, after eliminating the optic disc. This method successfully classified exudates in 93% of a dataset composed of 142 images.

## Chapter 3. System Architecture

---

After reviewing the literature pertaining to optic disc segmentation, and observing the conclusions related to each stage of the whole process, this chapter presents the proposed system architecture. The block diagram shown in the following figure illustrates the proposed architecture of optic disc segmentation, showing the data that was employed, the steps that were followed and the procedures that were applied in manipulating the eye fundus images [123].

PREVIEW IS NOT AVAILABLE

## Chapter 4. Experimental Results

---

PREVIEW IS NOT AVAILABLE

## Chapter 5. Conclusion and Future Work

---

PREVIEW IS NOT AVAILABLE

## Appendices

---

PREVIEW IS NOT AVAILABLE

## Ophthalmological Glossary

---

**Age-related Macular Degeneration (AMD):** a deterioration or breakdown of the eye's *macula* among people aged 50 and more. There are two types of macular degeneration: dry and wet. The most common type is the dry AMD where tiny yellow or white pieces of fatty protein called *drusen* form under the *retina*. Wet macular degeneration occurs when abnormal *blood vessels* begin to grow underneath the retina (i.e. *neovascularization*). These vessels can leak fluid and blood, which may lead to swelling and damage of the macula (i.e. *macular edema*).

**Aneurysms / Microaneurysms:** small bulges in *blood vessels* of the *retina* that often leak fluid.

**Arteriosclerosis:** a series of changes in the *retina* characterized by bleeding in the retina, thick fluid oozing from the retina, impaired oxygenation of the retina, an abrupt reduction of blood flow to the heart muscle that may cause dying off of tissue, and hardening of the walls of the little arteries (arterioles) in the eye.

**Blood vessels / vasculature:** the two main types of blood vessels responsible for the eye's blood supply are the arteries and veins. Arteries carry fresh blood from the heart and lungs to the eye while veins take away the blood that has been used by the eye and return it to the lungs and heart to be refreshed with oxygen and other nutrients. The arteries appear brighter and slightly narrower than the veins.

**Drusen:** tiny yellow or white pieces of fatty protein usually scattered around the *fovea* which is caused by *age-related macular degeneration*.

**Exudates:** deposits of cholesterol or other fats from the blood that have leaked into the *retina*. There are two types of exudates: hard exudates and soft exudates (also called cotton wool spots).

**Fovea:** a depression in the *retina* that contains only cones (not rods) and that provides accurate focused eyesight.

**Glaucoma:** a disease that damages the eye's optic nerve and can result in vision loss and blindness. It is characterized by the cupping of the *optic disc* which becomes ischemic due to the imbalance between the intraocular pressure and the perfusion pressure in the *blood vessels* of the *retina*.

**Hemorrhages:** a disorder of the eye in which bleeding leaks into the *retina* forming tiny blood spots.

**Macula:** a part of the eye close to the center of the *retina* responsible for central vision which allows us to see objects with great detail.

**Macular edema:** swelling or thickening of the *macula* caused by fluid leaking from the retinal *blood vessels*. The macula does not function properly when it is swollen.

**Neovascularization:** abnormal formation of new small *blood vessels* which contributes to visual loss in several ocular diseases, the most common of which are *proliferative diabetic retinopathy*, *age-related macular degeneration*, and *retinopathy of prematurity*.

**Non-proliferative Diabetic Retinopathy (NPDR):** the earliest stage of diabetic retinopathy. With this condition, damaged *blood vessels* in the *retina* begin to leak extra fluid causing *macular edema*, and small amounts of blood into the eye (i.e. *microaneurysms*). Sometimes, deposits of cholesterol or other fats from the blood may leak into the retina (i.e. *exudates*).

**Optic Disc (OD) / Optic Nerve Head (ONH):** a circular area where the optic nerve enters the *retina*; it does not contain receptors itself, and is thus the blind spot of the eye.

**Proliferative Diabetic Retinopathy (PDR):** a disease that mainly occurs when many of the *blood vessels* in the *retina* close, preventing enough blood flow. In an attempt to supply blood to the area where the original vessels closed, the retina responds by growing new blood vessels (i.e. *neovascularization*). However, these new blood vessels are abnormal and do not supply the retina with proper blood flow. The new vessels are also often accompanied by scar tissue that may cause the retina to wrinkle or detach (i.e. retinal detachment).

**Retina:** the tissue where the image is projected since it receives images formed by the lens and converts them onto signals that reach the brain by the means of the optic nerve. It contains light sensitive cells called cones and rods, which are responsible for daytime and night vision, respectively.

**Retinopathy of Prematurity:** a disease that affects immature *vasculature* in the eyes of premature babies. It can be mild with no visual defects, or it may become aggressive with new blood vessel formation (i.e. *neovascularization*) and progress to retinal detachment and blindness.

## References

---

- [1] K. Mahesh K. and K. Nilesh S., "Review on Fundus Image Acquisition Techniques with Database Reference to Retinal Abnormalities in Diabetic Retinopathy," *International Journal of Computer Applications*, vol. 68, no. 8, pp. 17-27, 2013.
- [2] X. Zhu, R. M. Rangayyan and A. L. Ells, "Digital Image Processing for Ophthalmology: Detection of the Optic Nerve Head," in *Synthesis Lectures on Biomedical Engineering*, Morgan & Claypool Publishers, 2011.
- [3] L. Segre, "Human Eye Anatomy - Parts of the Eye Explained," February 2013. [Online]. Available: <http://www.allaboutvision.com/resources/anatomy.htm>. [Accessed 15 July 2013].
- [4] Royal National Institute of Blind People (RNIB), *Retinal vessel occlusion*, 2013.
- [5] M. D. Abràmoff, M. K. Garvin and M. Sonka, "Retinal Imaging and Image Analysis," *IEEE Transactions on Medical Imaging*, vol. 3, pp. 169-208, 2010.
- [6] The University of British Columbia, "Ophthalmic Photography," Faculty of Medicine, Department of Ophthalmology & Visual Sciences, [Online]. Available: <http://ophthalmology.med.ubc.ca/patient-care/ophthalmic-photography/>. [Accessed 22 May 2015].
- [7] A. A. A. Youssif, A. Z. Ghalwash and A. A. S. A. Ghoneim, "Optic Disc Detection From Normalized Digital Fundus Images by Means of a Vessels' Direction Matched Filter," *IEEE Transactions on Medical Imaging*, vol. 27, no. 1, pp. 11-18, 2008.
- [8] *Retinal Image Computing and Understanding*.
- [9] N. Patton, T. M. Aslam, T. MacGillivray, I. J. Deary, B. Dhillon, R. H. Eikelboom, K. Yogesan and I. J. Constable, "Retinal image analysis: Concepts, applications and potential," *Progress in Retinal and Eye Research*, vol. 25, pp. 99-127, 2006.
- [10] R. C. Gonzalez and R. E. Woods, *Digital Image Processing*, Pearson Prentice Hall, 2008.
- [11] M. Goldbaum, "The STARE Project," 2000. [Online]. Available: <http://www.parl.clemson.edu/~ahoover/stare/index.html>. [Accessed 28 July 2013].

- [12] J. J. Staal, M. D. Abramoff, M. Niemeijer, M. A. Viergever and B. van Ginneken, "Ridge Based Vessel Segmentation in Color Images of the Retina," *IEEE Transactions on Medical Imaging*, vol. 23, pp. 501-509, 2004.
- [13] E. Decencière, X. Zhang, G. Cazuguel, B. Lay, B. Cochener, C. Trone, P. Gain, J. Ordonez-Varela, P. Massin, A. Erginay, B. Charton and J. Klein, "Feedback on a Publicly Distributed Database: The Messidor Database," *Image Analysis & Stereology*, vol. 33, no. 3, pp. 231-234, 2014.
- [14] J. Lowell, A. Hunter, D. Steel, B. Ryder and E. Fletcher, "Optic Nerve Head Segmentation," *IEEE Transactions on Medical Imaging*, vol. 2, no. 23, 2004.
- [15] Y. Zheng, M. H. A. Hijazi and F. Coenen, "Automated "Disease/No Disease" Grading of Age-Related Macular Degeneration by an Image Mining Approach," *Investigative Ophthalmology & Visual Science*, vol. 53, no. 13, pp. 8310-8318, November 2008.
- [16] D. J. J. Farnell, F. N. Hatfield, P. Knox, M. Reakes, S. Spencer, D. Parry and S. P. Harding, "Enhancement of blood vessels in digital fundus photographs via the application of multiscale line operators," *Journal of Franklin Institute*, vol. 345, no. 7, pp. 748-765, October 2008.
- [17] T. Kauppi, V. Kalesnykiene, J. Kamarainen, L. Lensu, I. Sorri, A. Raninen, R. Voutilainen, H. Uusitalo, H. Kalviainen and J. Pietila, "DIARETDB1 diabetic retinopathy database and evaluation protocol".
- [18] E. J. Carmona, M. Rincón, J. García-Feijoo and J. M. Martínez-de-la-Casa, "Identification of the Optic Nerve Head with Genetic Algorithms," *Artificial Intelligence in Medicine*, vol. 43, no. 3, pp. 243-259, 2008.
- [19] J. Odstrcilik, R. Kolar, A. Budai, J. Hornegger, J. Jan, J. Gazarek, T. Kubena, P. Cernosek, O. Svoboda and E. Angelopoulou, "Retinal vessel segmentation by improved matched filtering: evaluation on a new high-resolution fundus image database," *IET Image Processing*, vol. 7, no. 4, pp. 373-383, June 2013.
- [20] The MathWorks, "MATLAB," 2013.
- [21] Itseez, "OpenCV," 2015.
- [22] C. A. Schneider, W. S. Rasband and K. W. Eliceiri, "NIH Image to ImageJ: 25 Years of Image Analysis," *Nature Methods*, vol. 9, pp. 671-675, June 2012.
- [23] G. Dougherty, *Digital Image Processing for Medical Applications*, New York: Cambridge University Press, 2009.

- [24] F. ter Haar, "Automatic localization of the optic disc in digital colour images of the human retina," 2005.
- [25] N. Efford, *Digital Image Processing: A Practical Introduction Using Java*, Pearson Education, 2000.
- [26] M. Kass, A. Witkin and D. Terzopoulos, "Snakes: Active Contour Models," *International Journal of Computer Vision*, pp. 321-331, 1988.
- [27] T. F. Chan and L. A. Vese, "Active Contours Without Edges," *IEEE Transactions on Image Processing*, vol. 10, no. 2, pp. 266-277, 2001.
- [28] The MathWorks, Inc., "Marker-Controlled Watershed Segmentation," 2003. [Online]. Available: <http://www.mathworks.com/products/demos/image/watershed/ipexwatershed.html>. [Accessed 15 August 2013].
- [29] S. Beucher, "The Watershed Transformation page," 2010. [Online]. Available: <http://cmm.ensmp.fr/~beucher/wtshed.html>. [Accessed 15 August 2013].
- [30] G. T. Doran, "There's a S.M.A.R.T. way to write management's goals and objectives," *Management Review (AMA Forum)*, vol. 70, no. 11, pp. 35-36, 1981.
- [31] P. Macaskill, C. Gatsonis, J. Deeks, R. Harbord and Y. Takwoingi, "Analysing and Presenting Results," in *Cochrane Handbook for Systematic Reviews*, J. Deeks, P. Bossuyt and C. Gatsonis, Eds., The Cochrane Collaboration, 2010.
- [32] K. H. Zou, A. J. O'Malley and L. Mauri, "Receiver-Operating Characteristic Analysis for Evaluating Diagnostic Tests and Predictive Models," *Circulation*, vol. 115, pp. 654-657, 2007.
- [33] M. Kallergi, "Evaluation Strategies for Medical-Image Analysis and Processing Methodologies," in *The Electrical Engineering and Applied Signal Processing Series: Medical Image Analysis Methods*, L. Costaridou, Ed., Taylor & Francis Group, 2005.
- [34] M. M. Fraz, P. Remagnino, A. Hoppe, B. Uyyanonvara, A. R. Rudnicka, C. G. Owen and S. A. Barman, "Blood vessel segmentation methodologies in retinal images - A survey," *Computer Methods and Programs in Biomedicine*, vol. 108, no. 1, pp. 407-433, October 2012.
- [35] M. Lalonde, M. Beaulieu and L. Gagnon, "Fast and Robust Optic Disc Detection Using Pyramidal Decomposition and Hausdorff-Based Template Matching," *IEEE Transactions on Medical Imaging*, vol. 20, no. 11, pp. 1193-1200, November 2001.
- [36] S. Lu, "Accurate and Efficient Optic Disc Detection and Segmentation by a Circular Transformation," *IEEE Transactions on Medical Imaging*, vol. 30, no. 12, pp. 2126-2133, December 2011.

- [37] A. Aquino, M. E. Gegúndez-Arias and D. Marín, "Detecting the Optic Disc Boundary in Digital Fundus Images Using Morphological, Edge Detection, and Feature Extraction Techniques," *IEEE Transactions on Medical Imaging*, vol. 29, no. 11, pp. 1860-1869, November 2010.
- [38] L. Gagnon, M. Lalonde, M. Beaulieu and M.-C. Boucher, "Procedure to detect anatomical structures in optical fundus images," in *Proceedings of SPIE, Medical Imaging 2001: Image Processing*, 2001.
- [39] K. A. Goatman, A. D. Whitwam, A. Manivannan, J. A. Olson and P. F. Sharp, "Colour Normalisation of Retinal Images," in *Proceedings of Medical Image Understanding Analysis*, 2003.
- [40] F. A. Hashim, N. M. Salem and A. F. Seddik, "Preprocessing of Color Retinal Fundus Images," in *IEEE International Japan-Egypt Confernece on Electronics, Communications and Computers*, 6th of October City, 2013.
- [41] A. Hoover and M. Goldbaum, "Locating the Optic Nerve in a Retinal Image Using the Fuzzy Convergence of the Blood Vessels," *IEEE Transactions on Medical Imaging*, vol. 22, no. 8, pp. 951-958, 2003.
- [42] M. Goldbaum, S. Moezzi, A. Taylor, S. Chatterjee, J. Boyd, E. Hunter and R. Jain, "Automated diagnosis and image understanding with object extraction, object classification, and inferencing in retinal images," in *Proceedings of the IEEE International Conference on Image Processing*, 1996.
- [43] G. Yang, L. Gagnon, S. Wang and M.-C. Boucher, "Algorithm for detecting micro-aneurysms in low-resolution color retinal images," in *Proceedings of Vision Interface*, Ottawa, 2001.
- [44] M. Niemeijer, M. D. Abramoff and B. van Ginneken, "Fast detection of the optic disc and fovea in color fundus photographs," *Medical Image Analysis*, vol. 13, no. 6, pp. 859-870, December 2009.
- [45] N. M. Salem and A. K. Nandi, "Segmentation of Retinal Blood Vessels Using Scale-Space Features and K-Nearest Neighbour Classifier," in *Proceedings of the 2006 IEEE International Conference on Acoustics, Speech and Signal Processing*, Toulouse, 2006.
- [46] J. V. B. Soares, J. J. G. Leandro, R. M. Cesar Jr., H. F. Jelinek and M. J. Cree, "Retinal Vessel Segmentation Using the 2-D Gabor Wavelet and Supervised Classification," *IEEE Transactions on Medical Imaging*, vol. 25, no. 9, pp. 1214-1222, September 2006.
- [47] E. Ricci and R. Perfetti, "Retinal Blood Vessel Segmentation Using Line Operators and Support Vector Classification," *IEEE Transactions on Medical Imaging*, vol. 26, no. 10, pp. 1357-1365, October 2007.

- [48] A. Osareh and B. Shadgar, "Automatic Blood Vessel Segmentation in Color Images of Retina," *Iranian Journal of Science & Technology*, vol. 33, no. B2, pp. 191-206, 2009.
- [49] C. A. Lupascu, D. Tegolo and E. Trucco, "FABC: Retinal Vessel Segmentation Using AdaBoost," *IEEE Transactions on Information Technology in Biomedicine*, vol. 14, no. 5, pp. 1267-1274, June 2010.
- [50] M. M. Fraz, P. Remagnino, A. Hoppe, S. Velastin, B. Uyyanonvara and S. A. Barman, "A Supervised Method for Retinal Blood Vessel Segmentation Using Line Strength, Multiscale Gabor and Morphological Features," in *2011 IEEE International Conference on Signal and Image Processing Applications*, Kuala Lumpur, 2011.
- [51] M. M. Fraz, P. Remagnino, A. Hoppe and B. Uyyanonvara, "An Ensemble Classification-Based Approach Applied to Retinal Blood Vessel Segmentation," *IEEE Transactions on Biomedical Engineering*, vol. 59, no. 9, pp. 2538-2548, September 2012.
- [52] M. Al-Rawi, M. Qutaishat and M. Arrar, "An improved matched filter for blood vessel detection of digital retinal images," *Computers in Biology and Medicine*, vol. 37, pp. 262-267, 2007.
- [53] G. D. Finlayson, B. Schiele and J. L. Crowley, "Comprehensive Colour Image Normalization," in *Proceedings of the 5th European Conference in Computer Vision*, Freiburg, 1998.
- [54] W. Burger and M. J. Burge, *Digital Image Processing - An Algorithmic Introduction Using Java*, Springer London, 2008.
- [55] A. A. A. Youssif, A. Z. Ghalwash and A. S. Ghoneim, "A Comparative Evaluation of Preprocessing Methods for Automatic Detection of Retinal Anatomy," in *Proceedings of the 5th International Conference on Informatics & Systems*, Cairo, 2007.
- [56] A. A. S. A. Ghoneim, "Artificial Intelligence Techniques for Ocular Pattern Classification," Cairo, 2007.
- [57] D. Wu, M. Zhang, J. Liu and W. Bauman, "On the Adaptive Detection of Blood Vessels in Retinal Images," *IEEE Transactions on Biomedical Engineering*, vol. 53, no. 2, pp. 341-343, February 2006.
- [58] M. H. A. Fadzil, L. I. Izhar, H. Nugroho and H. A. Nugroho, "Analysis of retinal fundus images for grading of diabetic retinopathy severity," *Medical & Biological Engineering & Computing*, vol. 49, no. 6, pp. 693-700, January 2011.
- [59] M. R. Krishnan, U. R. Acharya, C. K. Chua, L. C. Min, E. Y. K. Ng, M. M. Mushrif and A. Laude, "Application of Intuitionistic Fuzzy Histon Segmentation for the Automated Detection of Optic Disc in Digital Fundus Images," in *Proceedings of IEEE-EMBS International Conference on Biomedical Health Informatics*, Hong Kong and Shenzhen, 2012.

- [60] M. Maruthusivarani, T. Ramakrishnan, D. Santhi and K. Muthukkutti, "Comparison of Automatic Blood Vessel Segmentation Methods in Retinal Images," in *2013 International Conference on Emerging Trends VLSI Embedded System, Nano Electronics and Telecommunication System*, Tiruvannamalai, 2013.
- [61] C. Sinthanayothin, J. F. Boyce, H. L. Cook and T. H. Williamson, "Automated localisation of the optic disc, fovea, and retinal blood vessels from digital colour fundus images," *British Journal of Ophthalmology*, vol. 4, no. 83, pp. 902-910, 1999.
- [62] A. Osareh, M. Mirmehdi, B. Thomas and R. Markham, "Classification and Localisation of Diabetic-Related Eye Disease," in *Proceedings of 7th European Conference on Computer Vision*, Copenhagen, 2002.
- [63] J. Park, K. N.T. and G. Lee, "Optic Disc Detection in Retinal Images using Tensor Voting and Adaptive Mean-Shift," in *2007 IEEE International Conference on Intelligent Computer Communication and Processing*, 2007.
- [64] C. Sinthanayothin, "Image Analysis for Automatic Diagnosis of Diabetic Retinopathy," 1999.
- [65] A. Polesel, G. Ramponi and V. J. Mathews, "Adaptive Unsharp Masking for Contrast Enhancement," in *Proceedings of the IEEE International Conference on Image Processing*, 1997.
- [66] M. N. Do and M. Vetterli, "The Contourlet Transform: An Efficient Directional Multiresolution Image Representation," *IEEE Transactions on Image Processing*, vol. 14, no. 12, pp. 2091 - 2106, December 2005.
- [67] P. Feng, Y. Pan, B. Wei, W. Jin and D. Mi, "Enhancing retinal image by the Contourlet transform," *Pattern Recognition Letters*, vol. 28, p. 516–522, 2007.
- [68] S. H. Rezaatofghi, A. Roodaki and H. Ahmadi Noubari, "An Enhanced Segmentation of Blood Vessels in Retinal Images Using Contourlet," in *30th Annual International Conference of the IEEE Engineering and Medicine Biology Society*, Vancouver, 2008.
- [69] M. S. Miri and A. Mahloojifar, "Retinal Image Analysis Using Curvelet Transform and Multistructure Elements Morphology by Reconstruction," *IEEE Transactions on Biomedical Engineering*, vol. 58, no. 5, pp. 1183-1192, May 2011.
- [70] G. Schaefer and A. Clos, "Image Analysis for Exudate Detection in Retinal Images," in *Biocomputation and Biomedical Informatics: Case Studies and Applications*, Medical Information Science Reference, 2010, pp. 198-203.

- [71] X. Zhu, R. M. Rangayyan and A. L. Ells, "Digital Image Processing for Ophthalmology: Detection of the Optic Nerve Head," in *Synthesis Lectures Biomed. Eng.*, Morgan & Claypool Publishers, 2011.
- [72] A. Dehghani, H. A. Moghaddam and M. Moin, "Optic disc localization in retinal images using histogram matching," *EURASIP Journal on Image and Video Processing*, vol. 19, pp. 1-11, October 2012.
- [73] P. C. Siddalingaswamy, "Automatic Detection of Retinal Features for Screening of Diabetic Retinopathy using Image Processing Techniques," 2011.
- [74] A. M. N. Allam, A. A. Youssif and A. Z. Ghalwash, "Automatic Segmentation of Optic Disc in Eye Fundus Images: A Survey," *Electronic Letters on Computer Vision and Image Analysis*, vol. 14, no. 1, pp. 1-20, September 2015.
- [75] M. Park, J. S. Jin and S. Luo, "Locating the Optic Disc in Retinal Images," in *Proceedings of the 3rd International Conference on Computer Graphics, Imaging and Visualization*, Sydney, Australia, 2006.
- [76] R. Chrástek, M. Wolf, K. Donath, G. Michelson and Niemann, "Optic Disc Segmentation in Retinal Images," in *Bildverarbeitung für die Medizin 2002*, Springer Berlin Heidelberg, 2002, pp. 263-266.
- [77] T. Walter and J. Klein, "Segmentation of Color Fundus Images of the Human Retina: Detection of the Optic Disc and the Vascular Tree Using Morphological Techniques," in *Proceedings of the 2nd International Symposium on Medical Data Analysis (ISMDA '01)*, 2001.
- [78] A. D. Abdel-Ghafar and T. Morris, "Progress towards automated detection and characterization of the optic disc in glaucoma and diabetic retinopathy," *Medical Informatics and the Internet in Medicine*, vol. 32, no. 1, pp. 19-25, March 2007.
- [79] X. Zhu, R. M. Rangayyan and A. L. Ells, "Detection of the Optic Nerve Head in Fundus Images of the Retina Using the Hough Transform for Circles," *Journal of Digital Imaging*, vol. 23, no. 3, pp. 332-341, June 2010.
- [80] M. Zubair, A. Yamin and S. A. Khan, "Automated Detection of Optic Disc for the Analysis of Retina Using Color Fundus Image," in *IEEE International Conference on Imaging Systems and Techniques*, Beijing, 2013.
- [81] C.-Y. Yu and S.-S. Yu, "Automatic Localization of the Optic Disc Based on Iterative Brightest Pixels Extraction," in *2014 International Symposium on Computer, Consumer and Control*, 2014.

- [82] A. D. Fleming, K. A. Goatman, S. Philip, J. A. Olson and P. F. Sharp, "Automatic detection of retinal anatomy to assist diabetic retinopathy screening," *Physics in Medicine and Biology*, vol. 52, no. 2, pp. 331-345, January 2007.
- [83] H. Ying, M. Zhang and J. Liu, "Fractal-based Automatic Localization and Segmentation of Optic Disc in Retinal Images," in *Proceedings of the 29th Annual International Conference of the IEEE EMBS*, 2007.
- [84] R. M. Rangayyan, X. Zhu, F. J. Ayres and A. L. Ells, "Detection of the Optic Nerve Head in Fundus Images of the Retina with Gabor Filters and Phase Portrait Analysis," *Journal of Digital Imaging*, vol. 23, no. 4, pp. 438-453, August 2010.
- [85] A. Osareh, M. Mirmehdi, B. Thomas and R. Markham, "Comparison of Colour Spaces for Optic Disc Localisation in Retinal Images," in *Proceedings of the 16th International Conference on Pattern Recognition*, 2002.
- [86] H. Li and O. Chutatape, "Automated Feature Extraction in Color Retinal Images by a Model Based Approach," *IEEE Transactions on Biomedical Engineering*, vol. 51, no. 2, pp. 246-254, February 2004.
- [87] M. Foracchia, E. Grisan and A. Ruggeri, "Detection of Optic Disc in Retinal Images by Means of a Geometrical Model of Vessel Structure," *IEEE Transactions on Medical Imaging*, vol. 23, no. 10, pp. 1189-1195, October 2004.
- [88] S. Lu, "Automatic Optic Disc Detection using Retinal Background and Retinal Blood Vessels," in *2010 3rd International Conference on Biomedical Engineering and Informatics*, Yantai, 2010.
- [89] D. Zhang and Y. Zhao, "Novel Accurate and Fast Optic Disc Detection in Retinal Images with Vessel Distribution and Directional Characteristics," *IEEE Journal of Biomedical Health Informatics*, no. 99, 28 October 2014.
- [90] The World Health Organization (WHO), "Fact sheet of visual impairment and blindness," [Online]. Available: <http://www.who.int/mediacentre/factsheets/fs282/en/>. [Accessed 30 June 2015].
- [91] H. A. Quigley and A. T. Broman, "The number of people with glaucoma worldwide in 2010 and 2020," *British Journal of Ophthalmology*, vol. 90, no. 3, pp. 262-267, 2006.
- [92] The Egyptian Society for the Glaucomas, [Online]. Available: <http://www.glaucoma-egypt.org/>. [Accessed 30 June 2015].
- [93] The American Academy of Ophthalmology, 2014.

- [94] The World Health Organization (WHO), "Fact sheet of diabetes," [Online]. Available: <http://www.who.int/mediacentre/factsheets/fs312/en/>.
- [95] M. Fingeret, F. A. Medeiros, R. Susanna and R. N. Weinreb, "Five rules to evaluate the optic disc and retinal nerve fiber layer for glaucoma," *Optometry*, vol. 76, no. 11, pp. 661-668, November 2005.
- [96] R. Thomas, K. Loibl and R. Parikh, "Evaluation of a Glaucoma patient," *Indian Journal of Ophthalmology*, vol. 59, no. 7, pp. 43-52, 2011.
- [97] R. Sihota, G. Srinivasan, T. Dada, V. Gupta, D. Ghate and A. Sharma, "Is the ISNT rule violated in early primary open-angle glaucoma - a scanning laser tomography study," *Eye*, vol. 22, pp. 819-824, 2008.
- [98] L. G. Nyul, "Retinal Image Analysis for Automated Glaucoma Risk Evaluation," *Proceedings of SPIE: Medical Imaging, Parallel Processing of Images and Optimization Techniques*, vol. 7497, pp. 1-9, October 2009.
- [99] R. R. A. Bourne, "The Optic Nerve Head in Glaucoma," *Community Eye Health Journal*, vol. 19, no. 59, pp. 44-45, 2006.
- [100] Z. Zhang, C. K. Kwok, J. Liu, C. Y. L. Cheung, T. Aung and T. Y. Wong, "Automatic Glaucoma Diagnosis with mRMR-based Feature Selection," *Journal of Biometrics & Biostatistics*, pp. 1-8, 2012.
- [101] Japan Glaucoma Society, "Guidelines for Glaucoma," Japan Glaucoma Society, Tokyo, 2006.
- [102] C. Muramatsu, Y. Hayashi, A. Sawada, Y. Hatanaka, T. Hara, T. Yamamoto and H. Fujita, "Detection of retinal nerve fiber layer defects on retinal fundus images for early diagnosis of glaucoma," *Journal of Biomedical Optics*, vol. 15, no. 1, pp. 1-7, February 2010.
- [103] T. Kubena, M. Kofronova and P. Cernosek, "Nerve Fiber Layer Defects Imaging in Glaucoma," in *The Mystery of Glaucoma*, T. Kubena, Ed., InTech, 2011, pp. 187-198.
- [104] European Glaucoma Society (EGS), Terminology and Guidelines for Glaucoma, 4th ed., PubliComm, 2014.
- [105] M. H. A. Fadzil, L. I. Izhar, H. Nugroho and H. A. Nugroho, "Analysis of retinal fundus images for grading of diabetic retinopathy severity," *Med Biol Eng Comput*, January 2011.
- [106] C. P. Wilkinson, F. L. Ferris, R. E. Klein, P. P. Lee, C. D. Agardh, M. Davis, D. Dills, A. Kampik, R. Pararajasegaram and J. T. Verdaguer, "Proposed International Clinical Diabetic Retinopathy and

- Diabetic Macular Edema Disease Severity Scales," *Ophthalmology*, vol. 110, no. 9, pp. 1677-1682, September 2003.
- [107] X. Song, K. Song and Y. Chen, "A Computer-based Diagnosis System for Early Glaucoma Screening," in *27th Annual Conference of Engineering in Medicine and Biology*, Shanghai, 2005.
- [108] Y. Hayashi, T. Nakagawa, Y. Hatanaka, A. Aoyama, M. Kakogawa, T. Hara, H. Fujita and T. Yamamoto, "Detection of Retinal Nerve Fiber Layer Defects in Retinal Fundus Images using Gabor Filtering," in *Proceedings of SPIE 6514, Medical Imaging 2007: Computer-Aided Diagnosis*, 2007.
- [109] C. Muramatsu, Y. Hatanaka, A. Sawada, T. Yamamoto and H. Fujita, "Computerized Detection of Peripapillary Chorioretinal Atrophy by Texture Analysis," in *33rd Annual International Conference of the IEEE EMBS*, Boston, 2011.
- [110] J. Liu, D. W. K. Wong, J. H. Lim, H. Li, N. M. Tan, Z. Zhang, T. Y. Wong and R. Lavanya, "ARGALI: An Automatic Cup-to-Disc Ratio Measurement System for Glaucoma Analysis Using Level-set Image Processing," in *13th International Conference on Biomedical Engineering (ICBME)*, 2009.
- [111] C. Burana-Anusorn, W. Kongprawechnon, T. Kondo, S. Sintuwong and K. Tungpimolrut, "Image Processing Techniques for GLaucoma Detection Using the Cup-to-Disc Ratio," *Thammasat International Journal of Science and Technology*, vol. 18, no. 1, pp. 22-34, 2013.
- [112] J. Nayak, A. U. R., P. S. Bhat, N. Shetty and T.-C. Lim, "Automated Diagnosis of Glaucoma using Digital Fundus Images," *Journal of Medical Systems*, vol. 33, pp. 337-346, 2009.
- [113] G. D. Joshi, J. Sivaswamy and S. R. Krishnadas, "Optic Disk and Cup Segmentation from Monocular Color Retinal Images for Glaucoma Assessment," *IEEE Transactions on Medical Imaging*, vol. 30, no. 6, pp. 1192-1205, 2011.
- [114] G. D. Joshi, J. Sivaswamy, P. Reddy and Krishnadas, "Detection of Peri-papillary Atrophy and RNFL Defect from Retinal Images," in *International Conference on Image Analysis and Recognition*, Hyderabad, 2012.
- [115] M. Madhusudhan, N. Malay, S. R. Nirmala and D. Samerendra, "Image Processing Techniques for Glaucoma Detection," in *Proceedings of 1st International Conference of Advances in Computing and Communications*, Kochi, 2011.
- [116] J. Cheng, Y. Xu, F. Yin, D. W. K. Wong, N.-M. Tan, D. Tao, C.-Y. Cheng, T. Aung and T. Y. Wong, "Superpixel Classification Based Optic Disc and Optic Cup Segmentation for Glaucoma Screening," *IEEE Transactions on Medical Imaging*, vol. 32, no. 6, pp. 1019-1032, 2013.

- [117] B. Harangi, B. Antal and A. Hajdu, "Automatic Exudate Detection with Improved Naïve-Bayes Classifier," in *2012 25th International Symposium on Computer-Based Medical Systems (CBMS)*, Rome, 2012.
- [118] H. F. Jaafar, A. K. Nandi and W. Al-Nuaimy, "Automated Detection and Grading of Hard Exudates from Retinal Fundus Images," in *19th European Signal Processing Conference*, Barcelona, 2011.
- [119] S. Kumar, R. Kumar, A. Sathar and V. Sahasranamam, "Automatic Detection of Exudates in Retinal Images Using Histogram Analysis," *2013 IEEE Recent Advances in Intelligent Computational Systems*, pp. 277-281, 2013.
- [120] A. Sopharak, K. T. Nwe, Y. A. Moe, M. N. Dailey and B. Uyyanonvara, "Automatic Exudate Detection with a Naive Bayes Classifier," *International Conference on Embedded Systems and Intelligent Technology*, pp. 139-142, 2008.
- [121] S. Sreng, J. Takada, N. Maneerat, D. Isarakorn, B. Pasaya, R. Panjaphongse and R. Varakulsiripunth, "Automatic Exudate Extraction for Early Detection of Diabetic Retinopathy," *2013 International Conference on Information Technology and Electrical Engineering*, pp. 31-35, 7-8 October 2013.
- [122] M. G. F. Eadgahi and H. Pourreza, "Localization of Hard Exudates in Retinal Fundus Image by Mathematical Morphology Operations," in *2nd International Conference on Computer and Knowledge Engineering*, 2012.
- [123] A. Osareh, M. Mirmehdi, B. Thomas and R. Markham, "Automated Identification of Diabetic Retinal Exudates in Digital Colour Images," *British Journal of Ophthalmology*, pp. 1220-1223, 2003.
- [124] A. M. N. Allam, A. A. Youssif and A. Z. Ghalwash, "Optic Disc Segmentation by Weighting the Vessels Density within the Strongest Candidates," in *IEEE SAI Computing Conference*, London, 2016.